The Dependence of the Predictability of Mesoscale Convective Systems on the Horizontal Scale and Amplitude of Initial Errors in Idealized Simulations

JONATHAN A. WEYN AND DALE R. DURRAN

Department of Atmospheric Sciences, University of Washington, Seattle, Washington

(Manuscript received 8 January 2017, in final form 10 April 2017)

ABSTRACT

Recent work has suggested that modest initial relative errors on scales of $O(100)$ km in a numerical weather forecast may exert more control on the predictability of mesoscale convective systems at lead times beyond about 5 h than 100% relative errors at smaller scales. Using an idealized model, the predictability of deep convection organized by several different profiles of environmental vertical wind shear is investigated as a function of the horizontal scale and amplitude of initial errors in the low-level moisture field. Small- and large-scale initial errors are found to have virtually identical impacts on predictability at lead times of 4–5 h for all wind shear profiles. Both small- and large-scale errors grow primarily up in amplitude at all scales rather than through an upscale cascade between adjacent scales. Reducing the amplitude of the initial errors improves predictability lead times, but this improvement diminishes with further reductions in the error amplitude, suggesting a limit to the intrinsic predictability in these simulations of slightly more than 6 h at scales less than 20 km. Additionally, all the simulated convective systems produce a $k^{-5/3}$ spectrum of kinetic energy, providing evidence of the importance of the unbalanced, divergent gravity wave component of the flow produced by thunderstorms in generating the observed atmospheric kinetic energy spectrum.

1. Introduction

The problem of mesoscale predictability in numerical weather forecasts is becoming increasingly important as computational resources allow the simulation of progressively finer-scale atmospheric features. It is also of societal importance, as the accurate prediction and localization of severe weather, including flash flooding and tornadoes, is vital to saving lives and property. Nearly 50 years ago, Edward Lorenz proposed the idea that certain deterministic fluid systems with many scales of motion, such as the atmosphere, have a finite range of predictability that cannot be extended by reducing the magnitude of the initial errors to any value greater than zero (Lorenz 1969). Although Lorenz provided a discussion of uncertainties caused by the flapping of seagull wings, which was eventually recast as the ''butterfly effect,'' he did not state that the initial errors constraining the intrinsic predictability of the atmosphere need to be small in scale. Indeed Lorenz's original paper described a pair of experiments suggesting that, at anything beyond extremely short forecast lead times, the ''intrinsic'' limits to predictability were insensitive to the horizontal scale of equal absolute-amplitude initial errors.

In the context of the Lorenz model for a system with a background kinetic energy (KE) spectrum that follows a $k^{-5/3}$ power law, where k is the horizontal wavenumber, the insensitivity to the scale of the initial errors arises because large-scale errors propagate downscale very rapidly (Rotunno and Snyder 2008), saturate the error in the smallest scales, and then propagate back up scale as if they had simply originated at small scales (Lorenz 1969). The practical importance of initial large-scale errors was emphasized by Durran and Gingrich (2014), who found that the initial-condition perturbations in hindcast convection-permitting ensemble simulations of East Coast snowstorms were strongest at the longest wavelengths, that those perturbations tended to grow simultaneously at all wavelengths rather than through an upscale cascade, and that the highly idealized Lorenz model could qualitatively reproduce such ''up amplitude'' error propagation if initialized with a roughly similar error spectrum.

Durran and Weyn (2016, hereafter DW16), tested whether the same insensitivity to the horizontal scale

Corresponding author: Jonathan A. Weyn, jweyn@uw.edu

DOI: 10.1175/JAS-D-17-0006.1

of initial errors might apply to deep moist convection, which is often thought to be particularly effective at transferring small-scale perturbations to larger scales (Zhang et al. 2006; Hohenegger and Schär 2007). DW16 compared the sensitivity of idealized squall-line simulations to the presence of initial potential temperature perturbations at wavelengths of 5.7 and 90 km and found the ensemble spread was somewhat more sensitive to perturbations at the longer wavelength. DW16 also showed that the idealized squall lines, growing in an environment with no background KE at any finite wavelength, were able to generate an ensemble-averaged background horizontal KE spectrum similar to the $k^{-5/3}$ spectrum observed in the atmosphere by aircraft at wavelengths less than about 400 km (e.g., Nastrom and Gage 1985; Lindborg 1999; Cho and Lindborg 2001). This result, which was confirmed by Sun et al. (2017), is particularly relevant to the study of mesoscale predictability because intrinsic limits to the predictability of idealized turbulent flows only occur when the system supports a background KE spectrum with a slope shallower than k^{-3} (Lorenz 1969; Rotunno and Snyder 2008). DW16 also suggested that neither the KE of the perturbations nor the background KE developed through a cascade in which the primary transfer of energy occurs between adjacent scales.

The goal of this paper is to assess the predictability of mesoscale convective systems (MCSs) as organized by varying amounts of vertical wind shear in an idealized horizontally homogeneous environment. The intrinsic predictability of the simulated storms is investigated by repeatedly reducing the magnitude of the initial errors. In all cases we consider ensemble simulations in which the surface and near-surface water vapor field is perturbed by the addition of either a large- or small-scale monochromatic square wave. We also examine the evolution of the background KE spectra produced by these systems, its distribution as a function of altitude, and the extent to which it is dominated by horizontally divergent or rotational flows.

The rest of the paper is organized as follows. Section 2 provides a detailed description of the model configuration and the initial state. Section 3 includes a description of the evolution of MCSs in different environments and the differences between ensemble members. Section 4 provides a discussion of the growth of errors in the simulations, while section 5 discusses dependence of predictability on the amplitude of the initial perturbations. Section 6 describes the decomposition of the wind fields into divergent and rotational components and their associated spectra. Completing the paper are a discussion in section 7 and conclusions in section 8.

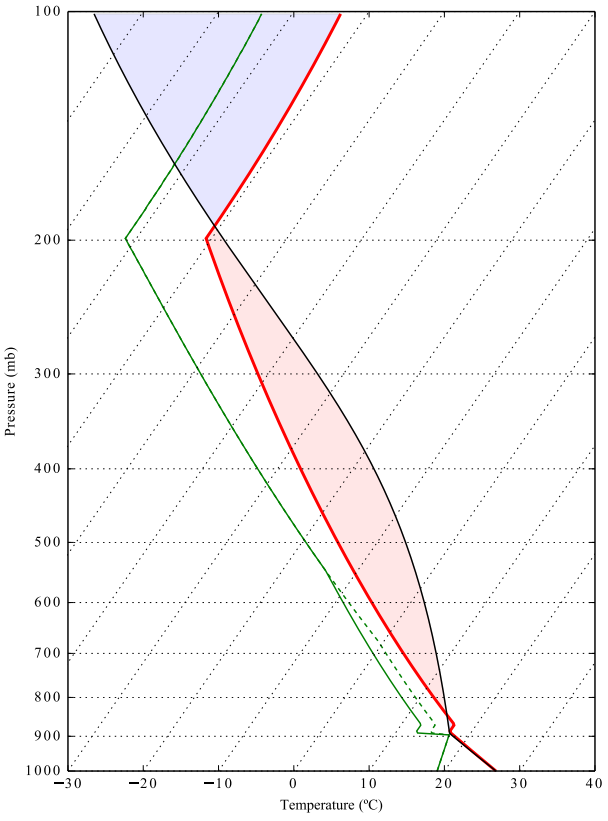

FIG. 1. Skew T–log$p$ plot of the thermodynamic sounding used to initialize the model simulations. The environmental temperature (red line), dewpoint with 75% cap above the boundary layer (solid green line), dewpoint with 85% cap above the boundary layer (dashed green line), and surface-based parcel temperature (black line) are shown. The "10" ensembles use the dashed dewpoint profile, while the "20" and "30" ensembles use the solid dewpoint profile.

2. Model configuration

A nonhydrostatic cloud-resolving model (Durran and Klemp 1983) is used to generate six ensembles of 20 members each. A pair of ensembles is produced for each of three different background vertical wind profiles consisting of unidirectional horizontal winds linearly increasing with height from 0 m s^{-1} at the surface to a maximum of 10, 20, and 30 m s^{-1} at a height of 5 km. The background thermodynamic profiles (Fig. 1) used in all three cases are similar to that of Weisman and Klemp (1982), but with a few changes made in an effort to simulate a more realistic severe weather environment. First, the temperature profile in the boundary layer is steepened such that the lapse rate is 9.5 K km^{-1} from the surface to 1 km. A shallow 300-m isothermal layer acts as a small capping inversion above the nearly dry adiabatic boundary layer. Second, the temperature profile follows (1) in Weisman and Klemp (1982) above the cap, except that the potential temperature of the

stratosphere at 12 km is decreased to 337 K. This increases the surface-based convective available potential energy (CAPE) to about 2800 $m^2 s^{-2}$ and slightly steepens the upper-tropospheric lapse rate. Third, the relative humidity profile follows (2) in Weisman and Klemp (1982), except that it is limited to 75% above the 1-km height of the boundary layer, where the equation would otherwise yield a higher value[1] (Wandishin and Stensrud 2008). Below 1 km, the water vapor mixing ratio is fixed at 14 g kg^{-1}. The combination of a well-mixed boundary layer, a shallow cap above the boundary layer with drier air, and a steeper upper-tropospheric lapse rate make this thermodynamic sounding more representative of severe weather environments (Bluestein 1993, 444–463).

Individual simulations are made on a 512 km × 512 km doubly periodic horizontal domain at 1-km horizontal resolution. There are 46 vertical levels from the ground to 17 km in height, with a vertical grid spacing of 40 m near the surface stretching to 500 m at 5 km above the surface. There is no upper damping layer; instead, gravity waves are radiated through the upper boundary using the formulation in Klemp and Durran (1983) and Bougeault (1983). A simple first-order-closure surface friction parameterization (Zhang and Anthes 1982; Gaberšek and Durran 2006) with surface momentum fluxes but no surface heat fluxes is used, which, along with the high near-surface vertical resolution, improves the treatment of cold pool dynamics and other boundary layer processes. A warm-rain Kessler microphysics scheme is used. There is no Coriolis force. The integration time step is 2 s, with an acoustic time step of 1 s, and the simulations are run for 6 h. In all ensemble members, three identical warm bubbles 2 K warmer than the environment produce the initial updrafts, which subsequently evolve into an organized MCS owing to the wind shear. The bubbles are spheroidal with a 10-km horizontal radius and 1.4-km vertical radius, centered 1.4 km above the surface and spatially located at (x, y) points of (100, 250), (125, 175), and (150, 300) km.

The methodology used to produce the ensembles is similar to that of DW16, but the perturbed field is the water vapor mixing ratio q_v instead of the potential temperature. To produce variability in the strength and position of the storms, initial perturbations of the form

$$q_v' = ae^{-z/H} \sin\left[2\pi\left(\frac{x}{L} - \phi_x\right)\right] \sin\left[2\pi\left(\frac{y}{L} - \phi_y\right)\right], \quad (1)$$

where a is the perturbation amplitude, H is the e-folding height scale, and L is the horizontal perturbation scale, are added to the background water-vapor field. The phases ϕ_x and ϕ_y ($0 \le \phi < 1$) are generated randomly for each ensemble member, and hence the differences between ensemble members originate in the difference in phase between the perturbations and the initial warm bubbles. Perturbing the moisture field has several important advantages over perturbing the potential temperature field. First, because water vapor perturbations contribute a much smaller fraction to vertical buoyancy forces than temperature perturbations, the moisture perturbations do not directly produce propagating waves. Second, by the same reasoning, the moisture perturbations have a much smaller effect on the difference between the surface-based CAPE of air parcels with positive perturbations versus those with negative perturbations. These advantages combine to reduce the likelihood of initiating spurious convection directly from the perturbations.

Each pair of ensembles consists of an "S" ensemble with L = 8 km and an "L" ensemble with L = 128 km to simulate the effects of small- and large-scale initial errors, respectively. It should be noted that, because of the square-wave structure of the perturbations, the true wavelengths of the perturbations are $2^{-1/2}L$ or about 5.7 and 90 km, respectively. The perturbation vertical scale height is H = 1 km, and the amplitude of the perturbations is a = 0.1 g kg^{-1} in all ensembles.[2] The six ensembles will hereinafter be referred to by the total amount of vertical wind shear (10, 20, or 30) and "S" or "L" to denote the perturbation scale. For example, the 20S ensemble is initialized with 20 m s^{-1} of total vertical wind shear and small-scale perturbations.

3. Evolution of MCSs and ensemble variability

Because of the different amounts of wind shear, the evolution of the MCSs produced in the ensemble simulations with 10, 20, and 30 m s^{-1} of vertical wind shear differs dramatically. What follows is a brief overview of the MCSs in each case intended to elucidate some differences in behavior.

When the vertical wind shear is 10 m s^{-1} (the "10" ensembles), the initial thunderstorms produced by the warm bubbles are stronger than those in the other ensembles. These storms dissipate about 2 h into the simulation as surface cold pool interactions and gust-front lifting produce the next round of convection. This second round

[1] To produce more sustained convection, this limit is only 85% in the 10 m s^{-1} shear sounding.

[2] With the exception of those with reduced perturbation amplitudes; see section 5.

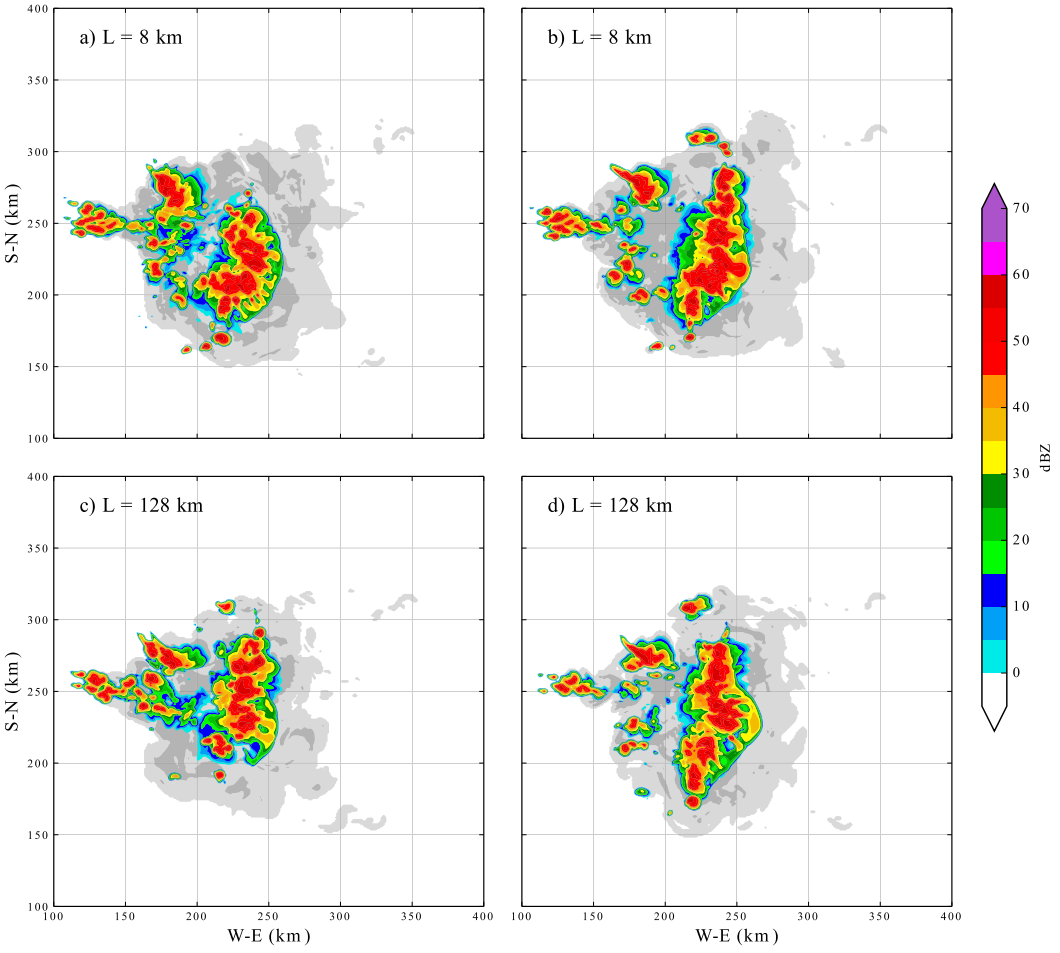

FIG. 2. Synthetic composite radar reflectivity (colors) and anvil-level (9–12 km) maximum cloud water content [contoured at 1×10^{-5} (light gray) and 1×10^{-1} g kg^{-1} (dark gray)] at 5 h for (a),(b) two members of the 10S ensemble and (c),(d) two members of the 10L ensemble. There is no active convection outside the plotted subdomain.

becomes an organized system with sustained gust-front lifting ahead of the main convective line and continues to strengthen over time. Scattered updrafts trail behind the main line. Figure 2 shows synthetic composite radar reflectivity for four different ensemble members in the "10" ensembles at 5 h into the simulations. Figures 2a and 2b show two members from the 10S ensemble, and Figs. 2c and 2d show two members from the 10L ensemble. The ensemble members were selected to show the greatest range of solutions among simulations produced by the introduction of the moisture perturbations.[3] Figures 2a and 2b show MCSs with comparatively shorter and longer north–south extent, respectively, and Figs. 2c and 2d show this difference mirrored in the 10L ensemble. Hence, the effect of the initial moisture perturbations on the MCSs is reflected similarly in the small- and large-scale ensembles.

When the wind shear is increased to 20 m s^{-1} (the "20" ensembles), the initial thunderstorms undergo splitting at around 1 h. The original cells slowly dissipate by about 3 h, producing a minimum in KE at that time as new convection begins to grow, again from cold pool interactions. The storm system strengthens as it organizes into a well-defined squall line by about 4.5 h. Similar variability is found among the members of the large- and small-scale ensembles as suggested in Fig. 3, which shows four "20" ensemble members in the same configuration as the previous figure. The comparatively shorter and longer squall lines in the two 20S ensemble members shown in Figs. 3a and 3b are mirrored in the two 20L ensemble members in Figs. 3c and 3d.

Finally, at the strongest shear of 30 m s^{-1} (the "30" ensembles), the initial thunderstorm cells likewise undergo a splitting sequence. Unlike in the other simulations, however, the initial cells do not dissipate, and instead new

[3] In each ensemble, the organization and distribution of the convective cells among all 20 members falls roughly evenly along a spectrum between the extremes illustrated in Figs. 2–4.

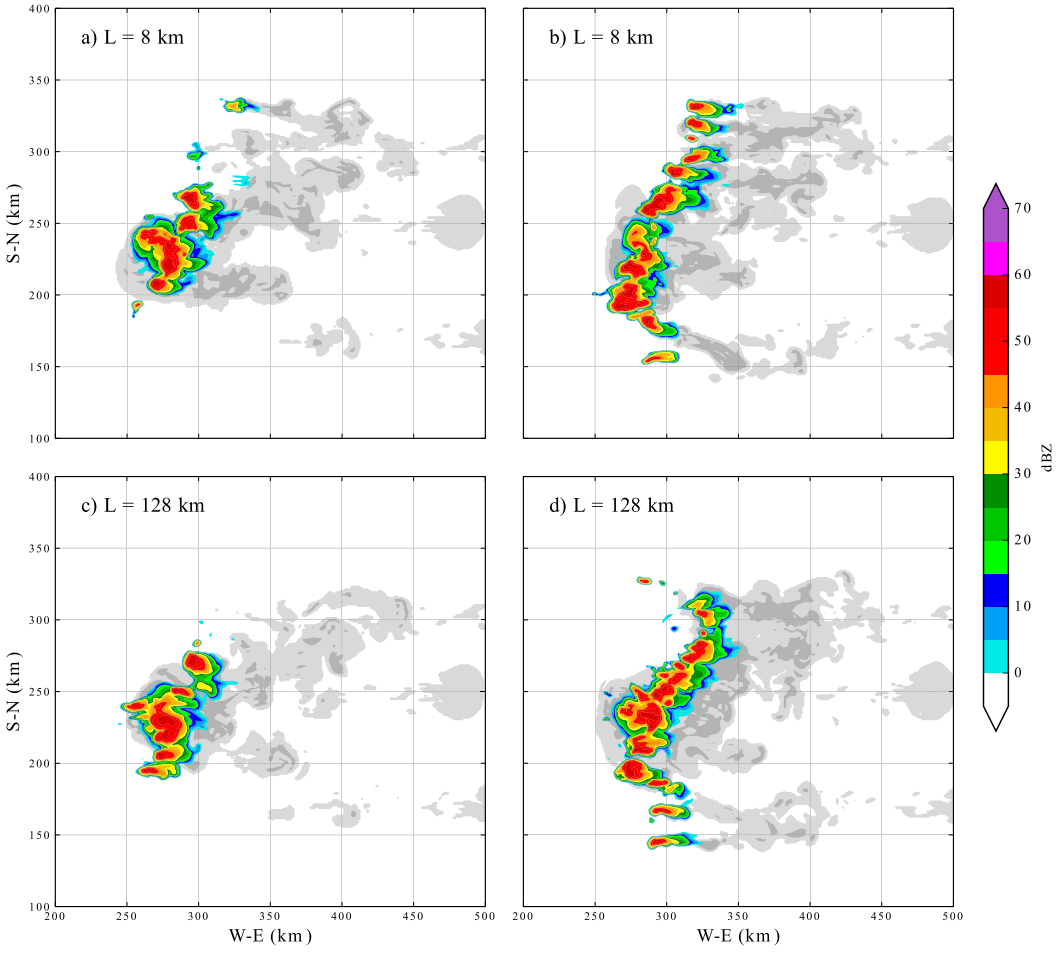

FIG. 3. As in Fig. 2, but for (a),(b) two members of the 20S ensemble and (c),(d) two members of the 20L ensemble.

convection builds up a strong squall line along the original cells. This squall line remains strong throughout the simulation and propagates over 400 km in 6 h, wrapping around the periodic domain. The 5-h composite reflectivity for four members is shown in Fig. 4, again in the same configuration as the previous two figures. The gross physical differences between the members of the 30S and 30L ensembles are much more subtle than those among the "10" and "20" ensembles, although there are small-scale variations in the locations of individual cells that, as will be discussed in the next section, keep the KE of the perturbation velocities about the ensemble mean quite large.

Sun et al. (2017) found that, in ensemble simulations of deep convection very similar to those in DW16 and this study, convective mixing results in a net loss of total KE in the mean flow. Figure 5 shows the evolution of the domain-averaged density-weighted KE, $(1/2)\rho(u^2 + v^2)$, normalized by the total density-weighted KE of the initial mean flow KE_B for comparison across ensembles with different vertical wind shear. A loss of total KE occurs in all ensembles, suggesting that the convection extracts energy from the mean flow (Sun et al. 2017). The convection in simulations with 30 m s^{-1} of wind shear is most efficient at reducing the normalized KE.

4. Growth of errors

To quantify the growth of the initial perturbations in the ensemble simulations, we analyze the spectra of total and perturbation (or error) horizontal KE. On the doubly periodic horizontal domain, the horizontal KE for a single ensemble member is calculated as follows. At a given height and time, denoting the zonal and meridional velocities of the mth ensemble member as u_m and v_m, respectively,[4] and denoting the two-dimensional

[4] The initial basic-state velocities are subtracted from the winds for all analyses. This makes no difference to the spectral analysis because the horizontally uniform basic state only has a wavenumber-0 component.

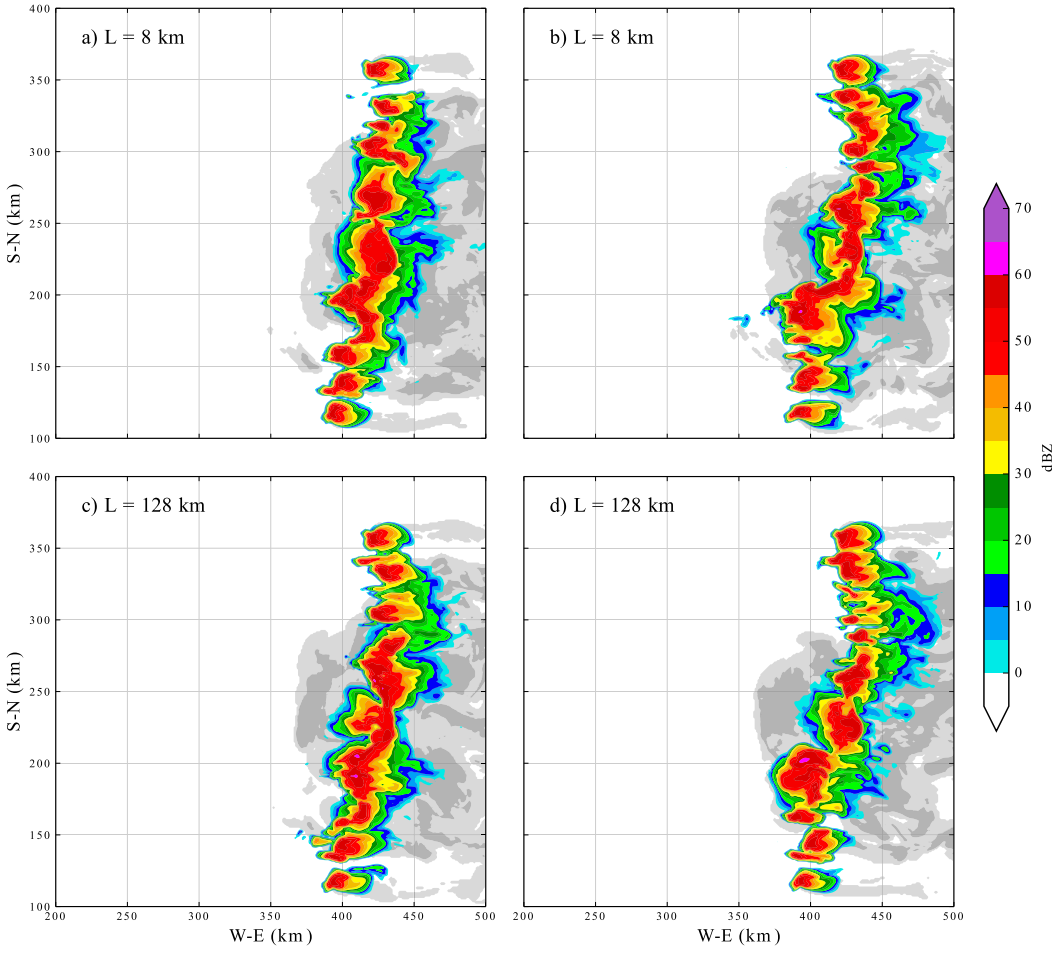

FIG. 4. As in Fig. 2, but for (a),(b) two members of the 30S ensemble and (c),(d) two members of the 30L ensemble.

discrete Fourier transform of a function ϕ as $\hat{\phi}$ and the complex conjugate as ϕ^*, the total (background) two-dimensional KE spectral density is

$$\widehat{\mathrm{KE}}_m(k_h) = \frac{\Delta x \Delta y \Delta k}{8\pi^2 n_x n_y}[\hat{u}_m(k_h)\hat{u}_m^*(k_h) + \hat{v}_m(k_h)\hat{v}_m^*(k_h)], \tag{2}$$

where k_h is the magnitude of the horizontal wavenumber, n_x and n_y are the number of grid points in the zonal and meridional directions, respectively, and Δx and Δy are the horizontal grid spacing in the zonal and meridional directions, respectively.[5] The spectral density at each individual horizontal wavenumber (k_x, k_y) is added to the bin for which $k_h - \Delta k/2 < \sqrt{k_x^2 + k_y^2} \le k_h + \Delta k/2$, where $\Delta k = 2\pi/512\,\mathrm{km}^{-1}$ is the smallest resolved wavenumber corresponding to a full-domain wave. The perturbation kinetic energy spectral density $\widehat{\mathrm{KE}}'_m$ is also calculated from (2), but the velocities are replaced by the difference from the ensemble mean: that is, $u'_m = u_m - \overline{u}$, where the overbar denotes the ensemble mean. The values of $\widehat{\mathrm{KE}}$ and $\widehat{\mathrm{KE}}'$ are then computed as the average of $\widehat{\mathrm{KE}}_m$ and $\widehat{\mathrm{KE}}'_m$ over all ensemble members.

Figure 6 shows the total and perturbation KE spectra for all six ensembles averaged over heights of 10–12 km, the level of thunderstorm anvil outflow.[6] Wavelengths shorter than 7 km ($7\Delta x$), indicated by shading, show a steep falloff of KE where numerical dissipation produces the strongest damping (Skamarock 2004). The

[5] The leading factor in (2) is appropriate for fast Fourier transforms computed using Matlab or Python, which are normalized through division by the total number of points in the inverse transform step [when $u(x)$ is recovered from $\hat{u}(k)$] (Durran et al. 2017, manuscript submitted to *Mon. Wea. Rev.*).

[6] As shown in Fig. 12, the anvil-outflow level is where KE is greatest and also roughly represents the same altitudes at which the atmospheric spectrum was measured (Nastrom and Gage 1985).

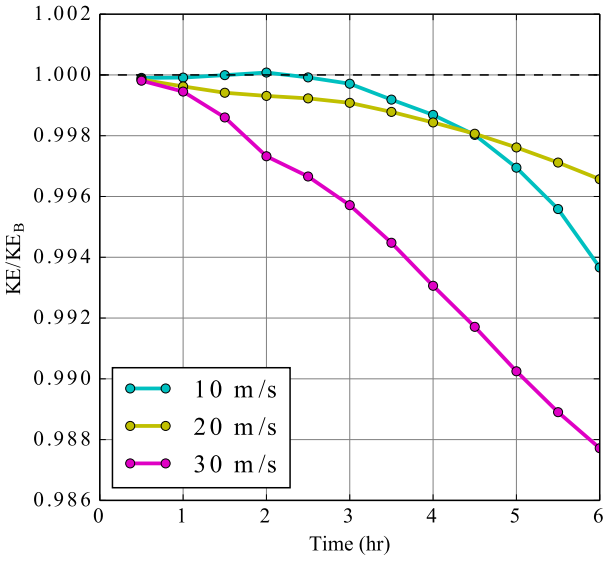

FIG. 5. Normalized domain-averaged density-weighted KE as a function of time for the 10L (cyan), the 20L (yellow), and the 30L ensembles (magenta) plotted every 30 min.

panels in each column correspond to the ensembles with different vertical wind shear, increasing from left to right, and those in the top (bottom) row correspond to the S (L) ensembles. The spectra of total KE, represented by solid lines at times of 1, 3, and 5 h, is similar in all ensembles and virtually identical between corresponding S and L pairs across the three vertical wind shear cases. At 1 h, the initial convection has produced a $k^{-5/3}$ KE spectrum for scales between about 7 and 60 km in all ensembles. By 5 h, the $k^{-5/3}$ spectrum extends to all resolved scales in all ensembles, indicating, as noted in DW16, that moist convection alone can produce a background KE spectrum whose slope matches that of the observed atmospheric mesoscale KE spectrum[7] (Nastrom and Gage 1985). Total KE is greatest in the "30" ensembles and least in the "20" ensembles.

The dashed lines in Fig. 6 show perturbation kinetic energy (KE′) at the same times as the total KE. Here, we observe an important difference in the 1-h spectra between corresponding S and L ensemble pairs. In the S ensembles, most notably in the 10S and 20S ensembles, there is a pronounced maximum in KE′ at wavelengths between about 10 and 30 km where the initial error has grown upscale from the initial perturbations at a wavelength of 5.7 km. KE′ falls off rapidly at wavelengths greater than about 30 km in the 10S and 20S ensembles and 50 km in the 30S ensemble. On the other hand, in the L ensembles, the large-scale initial errors at 90 km have interacted with neighboring scales to produce a relatively flat spectrum for all wavelengths above 10 km. Notably, in the L ensembles, the 1-h KE′ increases greatly with increasing environmental wind shear, while in the S ensembles, the 1-h KE′ generally decreases with increasing shear, except for the longest wavelengths in the 30S ensemble. At later times, the KE′ in all ensembles propagates primarily up-amplitude and secondarily upscale (Mapes et al. 2008; Durran et al. 2013; DW16). By 3 h, the KE′ spectra have filled the same scales and are similar in amplitude between S and L ensembles, while at 5 h, there is virtually no difference in KE′ or KE between S and L ensemble pairs. The KE′ spectra are very close to the KE spectra in all ensembles for wavelengths of less than about 30 km, then flatten out at larger scales,[8] indicating that predictability has been lost at wavelengths less than roughly 30 km.

To quantify this loss of predictability, we define the *error saturation* as the ratio of perturbation to total kinetic energy, KE′/KE, expressed as a percent. At a given scale, error saturation values near 100% indicate that there is no predictability, since the ensemble errors are as large as the ensemble mean. We choose a somewhat arbitrary threshold of 80% error saturation to indicate a significant loss of predictability, although, as noted by Potvin et al. (2017), even 100% error saturation need not imply a complete loss of subjective measures of forecast skill. Figure 7 shows spectra of error saturation at times of 1, 3, and 5 h in the S and L ensembles for each value of vertical wind shear. At 1 h, only the shortest wavelengths show any significant saturation in all six ensembles. By 3 h, wavelengths up to 10 km are about 80% saturated in the "10" ensembles, but the range of saturated wavelengths is less in the "20" ensembles and less still in the "30" ensembles. At a given wavelength, the values of KE′/KE in the 10L ensemble are less than those in the 10S ensemble at both 1 and 3 h. In the 20L ensemble, the error saturation is greater than that of the 20S ensemble at 1 h, but less at 3 h, and the values of KE′/KE in the 30L ensemble are greater than those in the 30S ensemble at both 1 and 3 h. In summary, while numerical artifacts may muddle the

[7] Waite (2016) found that the slopes of KE spectra in model simulations are sensitive to the model vertical resolution when $\Delta z \geq 500$ m. Sensitivity tests of 20L simulations with a vertical resolution of 200 m gave very similar spectra to those shown here.

[8] While the analysis presented here follows that of Lorenz (1969), a better measure of ensemble error in a realistic ensemble simulation is the mean difference from a control member, or "truth" state, instead of the ensemble mean. In this case, the errors saturate when KE′ = 2KE. Sensitivity tests where the errors about an unperturbed control run were used instead of the KE′ described here showed no qualitative difference in the analysis of error growth presented here.

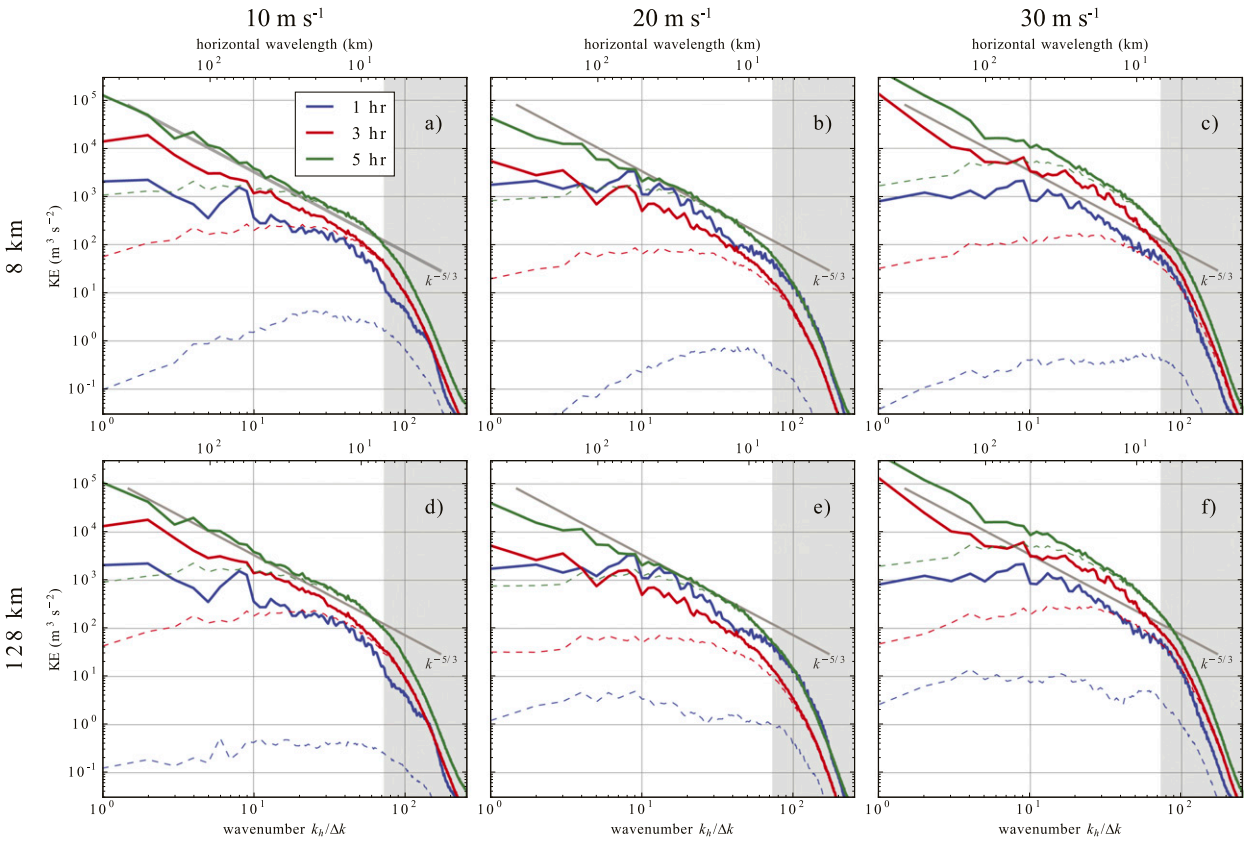

FIG. 6. Total (solid lines) and perturbation (dashed lines) KE spectral densities averaged over heights of 10–12 km for (a) the 10S, (b) the 20S, (c) the 30S, (d) the 10L, (e) the 20L, and (f) the 30L ensembles at 1 (blue), 3 (red), and 5 h (green) into the simulations. Also plotted in each panel is a reference $k^{-5/3}$ spectrum whose amplitude corresponds to that observed by Nastrom and Gage (1985). The gray shading indicates wavelengths smaller than numerical dissipation scales (see text).

behaviors of errors at very small scales, Fig. 7 indicates that increased environmental shear produces relatively less error saturation from small-scale errors than from large-scale errors in the earlier stages of the simulations. Nevertheless, by 5 h, the error saturation curves are nearly identical across all ensemble pairs. While difficult to determine from Fig. 7 because of the linear vertical axis, error saturation at scales larger than 200 km is about 2–5 times larger in the ''20'' ensembles than in the ''30'' ensembles (not shown). This supports the observation that the large-scale structure of the MCSs in the ''20'' ensembles (Fig. 3) shows greater variability among individual members than that in the ''30'' ensembles (Fig. 4).

The evolution of the error saturation for the specific wavelength range of 15–25 km is shown in Fig. 8. We choose this range of wavelengths because they are the largest waves that reach 80% saturation by 5 h in all ensembles (Fig. 7). The errors clearly saturate fastest in the ''10'' ensembles and slowest in the ''30'' ensembles. Additionally, the simulations with initial small-scale errors (dotted lines) in the ''10'' and ''20'' ensembles saturate faster than those with initial large-scale errors, while the simulations with initial large-scale errors (dashed lines) in the ''30'' ensembles saturate faster than those with initial small-scale errors, consistent with the conclusions from Fig. 7. Nevertheless, between 4.5 and 5 h, each of the ensemble pairs develops the same amount of error saturation, or loss of predictability.

Early evolution of errors in a developed flow

As we noted earlier, errors (KE′) grow up-amplitude in time [see also DW16 and Potvin et al. (2017)]. We also describe in the introduction the mechanism by which large- and small-scale initial errors produce nearly identical patterns of upscale error growth in the Lorenz model. Is this behavior observable in the present simulations of MCSs? The notion of a rapid downscale propagation and subsequent saturation of errors on small scales is difficult to assess in the simulations presented above because the convection must produce the background (total) KE spectrum at the same time the errors are building. To better separate the amplitudes of the KE

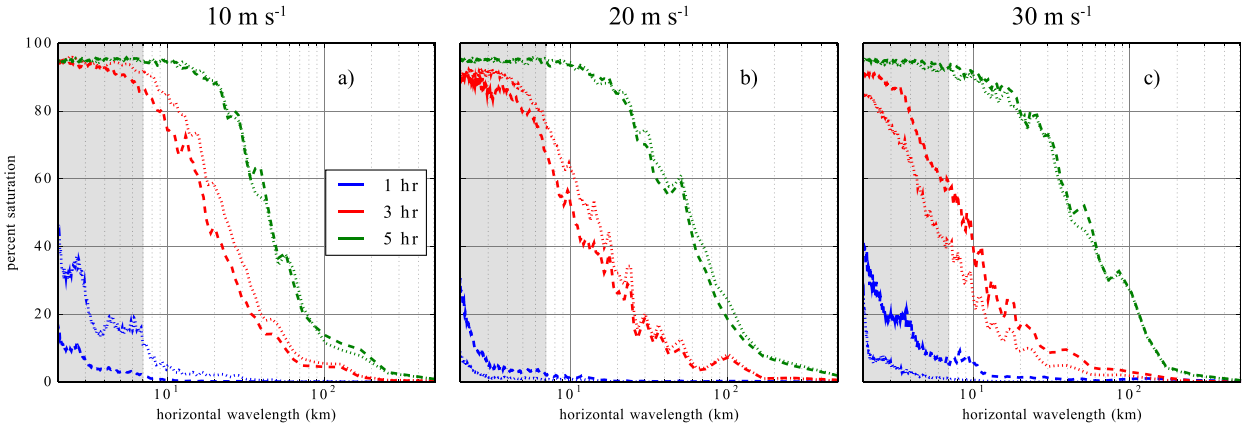

FIG. 7. Error saturation (the ratio of perturbation to total kinetic energy: KE′/KE; %) averaged over heights of 10–12 km for the (a) "10," (b) "20," and (c) "30" ensembles at 1 (blue), 3 (red), and 5 h (green) into the simulations. The S (L) ensembles are represented by dotted (dashed) lines. For ease of interpretation, the horizontal axis is wavelength. The gray shading is as in Fig. 6.

and initial KE′ spectra, two additional ensembles with $20\,\mathrm{m\,s^{-1}}$ of wind shear were run in which the moisture perturbations were introduced at 1 h into the simulations when the background KE spectrum is already well developed and growing more slowly (recall Fig. 6). These ensembles are denoted "20S1" and "20L1" for small-scale and large-scale perturbations, respectively.

Figure 9 shows the KE′ spectra from the 20S1 and 20L1 ensembles, vertically averaged over $0 \le z \le 16$ km, at times 3, 6, and 12 min after the first errors were introduced. Also plotted is the average background KE over the same time period. The most noticeable features of the KE′ spectra are the peaks at 5.7 and 90 km where the moisture (but no velocity or temperature) perturbations were introduced in the 20S1 and 20L1 ensembles, respectively. At 1 h 3 min, KE′ is larger in the 20S1 ensemble than in the 20L1 ensemble at scales less than 10 km, while at scales larger than 10 km, the 20L1 errors have filled the spectrum more than the 20S1 errors. Nevertheless, the large-scale errors in the 20L1 ensemble propagate to even the smallest scales within just 3 min. The small-scale errors grow sufficiently rapidly in the 20L1 ensemble that, within 12 min, the 20L1 KE′ is actually somewhat larger than the 20S1 KE′ at almost all scales. Although the initial errors spread rapidly across scales, their early growth does not follow a strict upscale or downscale cascade. Instead, in both ensembles, scale interactions tend to flatten the KE′ spectra rather quickly and produce simultaneous up-amplitude growth at all scales.

5. Sensitivity to perturbation strength

The $0.1\,\mathrm{g\,kg^{-1}}$ amplitude for the initial moisture perturbations was chosen somewhat arbitrarily. In the highly nonlinear flow generated by mesoscale convective systems, it is not obvious how the predictability lead time will respond to changes in the perturbation amplitude. To investigate this, we introduce two new pairs of S and L ensembles with the $20\,\mathrm{m\,s^{-1}}$ wind shear profile and perturbation amplitudes reduced by factors of 5 ($a = 0.02\,\mathrm{g^{-1}}$) and 25 ($a = 0.04\,\mathrm{g^{-1}}$) compared to the original amplitude. We will denote these ensembles by appending "/5" or "/25" such that the ensemble with initial amplitude a/25 and perturbation scale $L = 8$ km is named 20S/25.

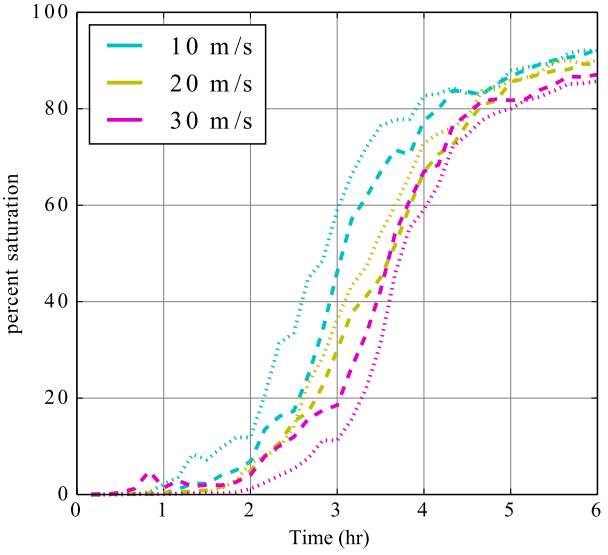

FIG. 8. Error saturation (KE′/KE; %) averaged over heights of 10–12 km, summed over horizontal wavelengths of 15–25 km, for the 10S (dotted cyan), 10L (dashed cyan), 20S (dotted yellow), 20L (dashed yellow), 30S (dotted magenta), and 30L (dashed magenta) ensembles.

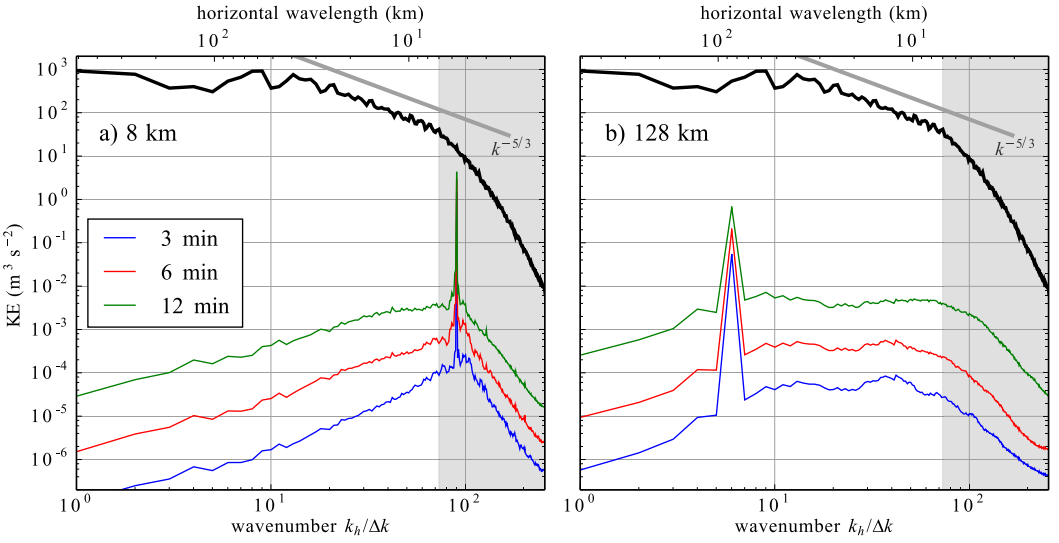

FIG. 9. Perturbation kinetic energy (KE′; thin solid lines) at 3, 6, and 12 min after the introduction of errors at 1 h in the (a) 20S1 and (b) 20L1 ensembles, vertically averaged between 0 and 16 km. The thick black line shows the total KE averaged over the same period (from 1 h 3 min to 1 h 12 min). The gray shading and gray $k^{-5/3}$ reference line are as in Fig. 6.

Figure 10 shows spectra of the error saturation KE′/KE similar to those in Fig. 7, but with varying *a* instead of varying amounts of vertical wind shear. Curves for 1, 3, and 5 h are plotted in each panel. The error saturation values at 1-h decrease dramatically as *a* decreases, becoming essentially negligible on a linear scale in the "/5" and "/25" ensembles. At 3 h, scales of 10 km are about 60% saturated in the original "20" ensembles, but are only about 30% and 20% saturated for the "/5" and "/25" ensembles, respectively. By 5 h, scales of 20 km are about 85% saturated in both "20" ensembles, 75% saturated in both "/5" ensembles, and 70% saturated in both "/25" ensembles. Although it takes somewhat longer for the "/5" and "/25" ensembles to achieve 80% error saturation, and thereby the same loss of predictability, as for the original "20" ensembles, the increase in predictability diminishes as the initial errors are made smaller. Moreover, for all three initial amplitudes, the predictability at 5 h is the same for both small- and large-scale initial errors.

An alternate illustration of this time dependence is provided in Fig. 11, where the average error saturation spectrum for all 40 members of the "20," "/5," and "/25" ensembles is plotted at different times, chosen to most closely match the 6-h error saturation spectrum of the "/25" ensembles. The "20," "/5," and "/25" ensembles have similar error saturation spectra at 290, 340, and 360 min, respectively. Thus, the first reduction of the

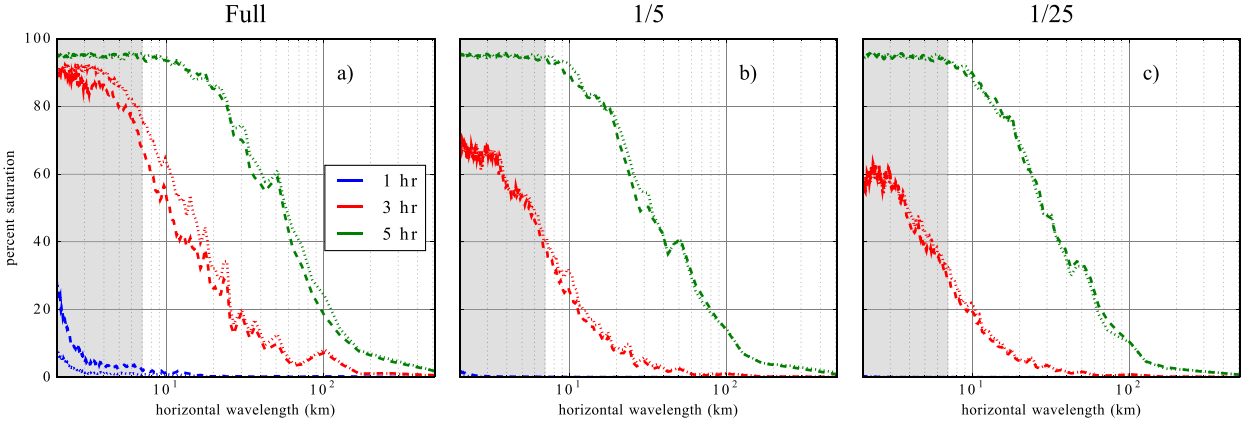

FIG. 10. Error saturation (KE′/KE; %) averaged over heights of 10–12 km for the "20" ensembles with (a) the full initial-amplitude perturbations, and with those perturbations reduced by a factor of (b) 1/5 and (c) 1/25. Data are plotted at times 1 (blue), 3 (red), and 5 h (green) into the simulations. The S (L) ensembles are represented by dotted (dashed) lines. The gray shading is as in Fig. 6.

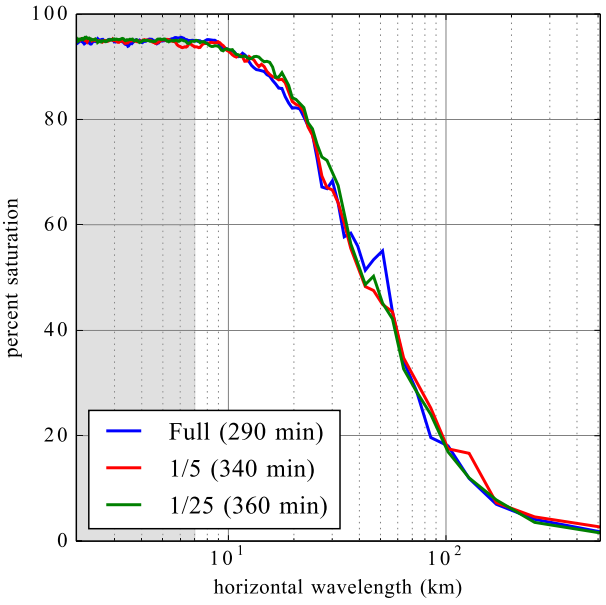

FIG. 11. Error saturation (KE′/KE; %) averaged over heights of 10–12 km for the "20" ensembles at 290 min (blue), the "/5" ensembles at 340 min (red), and the "/25" ensembles at 360 min (green). All 40 members in the ensemble pairs were averaged for clarity. The times were chosen to most closely match the 360-min spectrum in the "/25" ensembles.

perturbation amplitude by a factor of 5 resulted in an extra 50 min of predictability lead time, or the simulation time required to attain a particular spectrum of error saturation, while a further reduction of the perturbation amplitude by another factor of 5 resulted in only 20 min of additional predictability lead time.

The sensitivity of predictability lead time to initial-error amplitude in these simulations agrees with that in the highly idealized model of Lorenz (1969). When the background KE spectrum has a $k^{-5/3}$ slope, the Lorenz model predicts initially unsaturated errors will propagate rapidly downscale (Lorenz 1969; Rotunno and Snyder 2008), and if the amplitude of the initial error is decreased, as in Lorenz's experiment C, the scale that first saturates though downscale propagation becomes smaller. Because the eddy turnover time decreases with decreasing length scale (Lorenz 1969; Rotunno and Snyder 2008), the subsequent upscale error propagation proceeds more rapidly at smaller scales, leading to diminishing gains in the predictability lead time with decreasing initial-error amplitude. Nevertheless, although the predictability lead time in our simulations is determined by the absolute amplitude of the initial errors, independent of their horizontal scale, the errors in our simulations do not evolve through a cascade in which they are primarily transferred between adjacent scales; instead, the errors tend to increase simultaneously at all scales (up-amplitude growth) while spreading rapidly across all scales.

6. Decomposition into divergent and rotational components

To provide insight into the mechanics of the KE spectra generated by the simulated storms, we decompose the horizontal wind fields and KE into divergent and rotational parts as in Waite and Snyder (2013). Using spectral derivatives of Fourier-transformed velocities (from which the mean flow has been subtracted), for the mth ensemble member, the vorticity is $\hat{\zeta}_m(k_x, k_y) = ik_x\hat{v}_m - ik_y\hat{u}_m$ and the divergence is $\hat{\delta}_m(k_x, k_y) = ik_x\hat{u}_m + ik_y\hat{v}_m$. The divergent kinetic energy (DKE) spectrum is then given by

$$\widehat{\mathrm{DKE}}_m(\mathbf{k}) = \frac{1}{2}\frac{\hat{\delta}_m(\mathbf{k})\hat{\delta}_m^*(\mathbf{k})}{k_h^2},$$

and the rotational kinetic energy (RKE) spectrum is computed from

$$\widehat{\mathrm{RKE}}_m(\mathbf{k}) = \frac{1}{2}\frac{\hat{\zeta}_m(\mathbf{k})\hat{\zeta}_m^*(\mathbf{k})}{k_h^2}.$$

Because there is no Coriolis force in the simulations, there is no large-scale balanced rotational flow, and both the divergent and rotational wind components develop as a result of the convection. Vertical profiles of ensemble-mean wavenumber-integrated total KE, DKE, and RKE at 5 h for each L ensemble[9] are shown in Figs. 12 and 13. To compensate for the differences in the horizontal extent of the MCSs that develop in different environments, these profiles have been normalized by the number of horizontal points in the domain with ensemble-mean KE greater than 1 $\mathrm{m^2\,s^{-2}}$.

We first consider KE summed over all horizontal wavelengths longer than 32 km, for which several prominent features appear in the profiles in Fig. 12. First, there is a pronounced maximum in KE at the thunderstorm-anvil-outflow level (10–12 km) dominated by the divergent component. Second, there is a secondary maximum just above the surface as a result of the dynamics of the surface cold pool spreading, also dominated by the divergent component, that is, however, nearly absent in the 30L ensemble. Third, there are alternating levels between the surface and the tropopause (12 km) where the DKE is larger than the RKE and vice versa; these are discussed further below. Finally, the RKE, for scales larger than 32 km, becomes increasingly large at all levels as the environmental wind

[9] As suggested by Fig. 6, the differences between the L and S ensembles at 5 h are negligible.

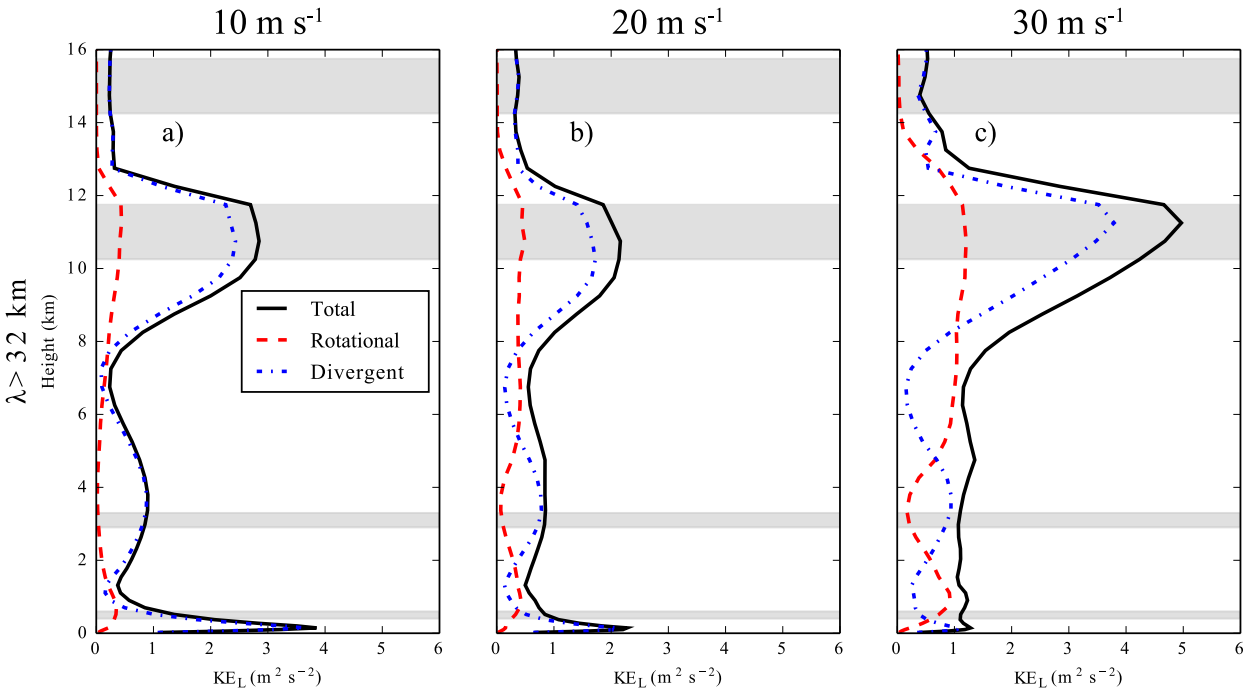

FIG. 12. Vertical profiles of horizontal KE of the total wind field (solid black lines), divergent wind field (dotted–dashed blue lines), and rotational wind field (dashed red lines) for (a) the 10L, (b) the 20L, and (c) the 30L ensembles at 5 h. KE_L represents the sum of KE over wavenumbers larger than 32 km. The values of KE have been normalized by the average number of horizontal grid points at the anvil level (10–12 km) where KE of the ensemble-mean winds minus the background vertical wind profile is greater than 1 $m^2 s^{-2}$. The gray shaded areas correspond to the vertical intervals from which data are collected for Figs. 14–20.

shear increases: the stronger storms under higher shear produce more vertical vorticity, as localized updrafts tilt environmental vorticity into the vertical. Note also that the maximum in the vertical distribution of KE in the 30L ensemble bears some resemblance to the KE distribution in the single supercell simulation in an environment with 40 $m s^{-1}$ shear in Lilly et al. (1998, their Fig. 8a), except that the KE below the anvil-outflow level in the supercell simulation was almost negligible.

Figure 13 again shows vertical profiles of KE, DKE, and RKE, but for disturbances with wavelengths shorter than 32 km. At these shorter wavelengths, there is much less total KE, as expected from the slope of the background KE spectrum. In contrast to the long-wavelength velocities shown in Fig. 12, at scales less than 32 km, the RKE is comparable to the DKE in the 10L ensemble and larger in the 20L and 30L ensembles, except at the surface and in the stratosphere above the anvil-outflow level. This is evidence of the important contribution to the RKE of the vortices produced by individual convective cells, which strengthen with increasing wind shear. The DKE, on the other hand, shows little variation in either magnitude or vertical structure with increasing wind shear.

Vertical levels and layers of particular interest are highlighted by gray in Figs. 12 and 13: these are within the gust front ($z = 0.5$ km), the rear-inflow jet ($z = 3$ km), the anvil-outflow layer ($10 \leq z \leq 12$ km), and the lower stratosphere ($14 \leq z \leq 16$ km). At the height of $z = 0.5$ km above the surface, there is a maximum in large-scale divergent winds as a result of cold pool spreading under the convection. This is illustrated in Fig. 14, which shows the large-scale (>32 km) divergence and rotational winds at this height at 5 h for the member from the 10L, 20L, and 30L ensembles shown in Figs. 2d, 3d, and 4d, respectively. There is also a rotational signature of bookend vortices and rear-to-front flow into the squall line, which is a typical feature of such systems (e.g., Weisman and Trapp 2003; Trapp and Weisman 2003). Figure 15 shows the 5-h spectra of KE, DKE, and RKE for each L ensemble at $z = 0.5$ km. These spectra show that the DKE is about 2–3 times larger than the RKE in the 10L and 20L ensembles over wavelengths between $7\Delta x$ and about 100 km. In contrast, the DKE and RKE are comparable in the 30L ensemble, except for wavelengths shorter than about 20 km, where the DKE is larger. In all cases, the DKE and RKE both follow an approximate $k^{-5/3}$ spectrum over wavelengths of $7\Delta x$ to about 100 km.

At $z = 3$ km, the DKE exceeds the RKE at scales larger than about 15, 30, and 70 km in the 10L, 20L, and 30L ensembles, respectively (Fig. 16). Interestingly, the DKE

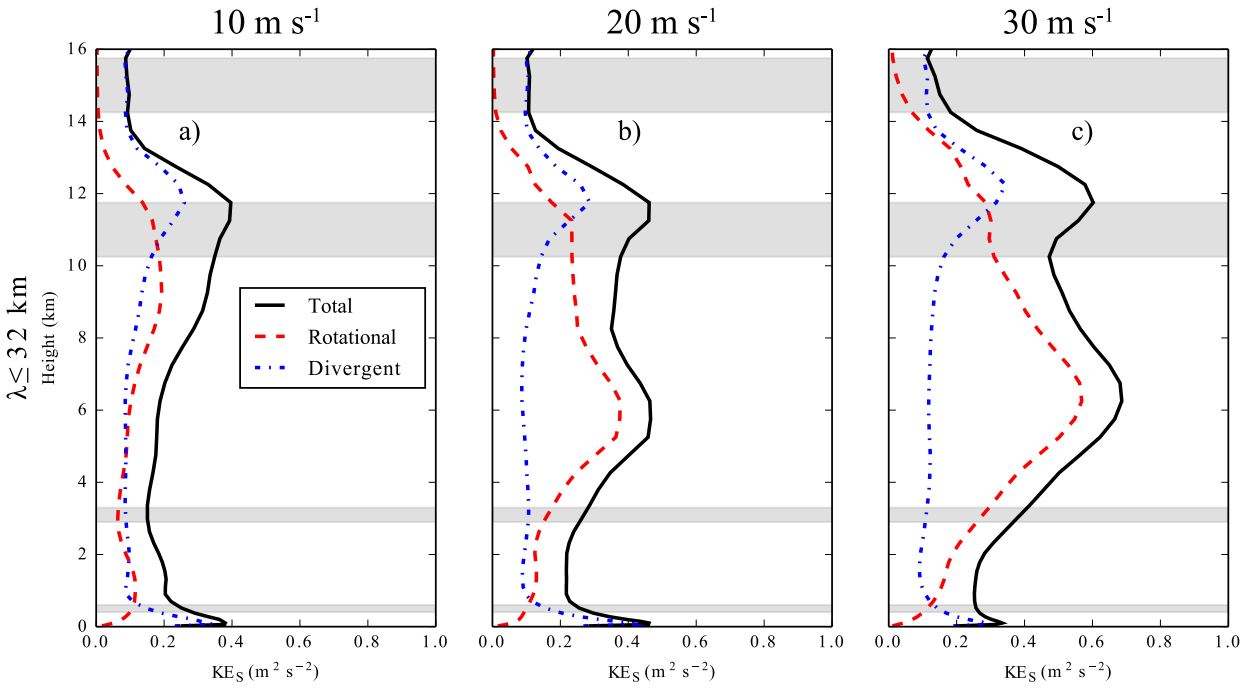

FIG. 13. As in Fig. 12, but KE_S represents the sum of KE over wavenumbers less than or equal to 32 km.

follows a $k^{-5/3}$ spectrum across the resolved scales, while the slope of the RKE is steeper at very small scales and flattens out at large scales. Consistent with the vertical profiles plotted in Figs. 12 and 13, the RKE is strongest in the 30L ensemble, which has the highest vertical wind shear.

At the anvil-outflow level, the total KE is at its maximum. Strong upper-level divergence occurs on a scale larger than the MCS itself, as shown by the horizontal divergent winds at a height of 11 km in Figs. 17a–c. The rotational wind field at this same level exhibits a pronounced mesoscale front-to-rear rotational flow through the MCSs, with two main counterrotating vortices (Figs. 17d–f). The KE spectra averaged over $10 \le z \le 12$ km, plotted in Fig. 18, show the DKE exceeds the RKE at sufficiently long wavelengths in all ensembles, accounting for the dominance of DKE over RKE apparent in Fig. 12 in the anvil-outflow layer. In contrast to the RKE, the slope of the DKE approximates a $k^{-5/3}$ spectrum at all wavelengths not significantly impacted by numerical dissipation.

In the stratosphere, the horizontal velocities and the KE values are much smaller than those at the anvil-outflow level. At 14 km, the divergent winds exhibit clear features of gravity waves, particularly in the pronounced circular symmetry in the 10L simulation (Fig. 19a). The stratospheric KE, averaged between heights of 14 and 16 km, is largely dominated by the DKE of these gravity waves, which is over an order of magnitude stronger than the RKE at all scales in the 10L and 20L ensembles and about 2–3 times larger in the 30L ensemble (Fig. 20).

Our 20 m s^{-1} shear cases are similar to the simulations conducted in Sun et al. (2017), and the slopes of their DKE and RKE spectra averaged over 0–15 km and 4–6 h (see their Fig. 6), are similar to those of the spectra from our 20L simulation averaged over the same times and vertical levels and vertically weighted by density (Fig. 21). But in contrast to our results, in Sun et al. (2017) the RKE exceeds the DKE for all wavelengths shorter than 180 km, and for a broad range of those wavelengths the difference is roughly a factor of 2. As shown in Fig. 21, we find the DKE and RKE have very similar magnitudes for all well-resolved wavelengths shorter than 40 km and that the DKE exceeds the RKE on all scales greater than 40 km. The biggest difference between our simulations and those in Sun et al. (2017) appears to be their use of seven warm bubbles with perturbation temperatures of 3 K to trigger the initial convection instead of our three warm bubbles with 2-K temperature perturbations, although it is not obvious how this difference should affect the relative strength of the RKE and DKE spectra.

Unlike the real atmosphere, there is no source of KE at large scales in our simulations, in which the background environment is horizontally homogeneous, our 512 km × 512 km domain is relatively small, and Coriolis forces are neglected. As a consequence, the spectral power in the longest wavelengths is not enhanced by downscale energy propagation from the synoptic scales. Nevertheless, several characteristics of our

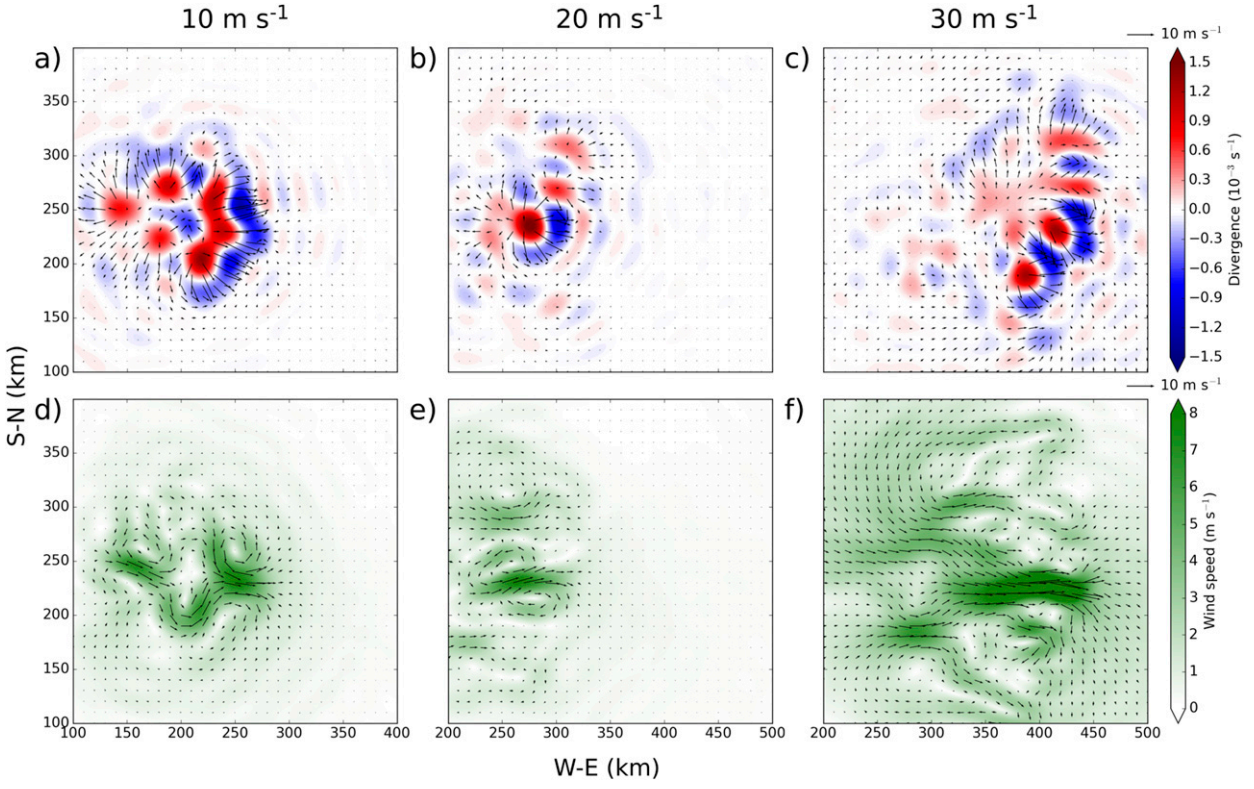

FIG. 14. (a)–(c) Horizontal divergence (colors) and divergent wind vectors for a selected member of the (left) 10L, (center) 20L, and (right) 30L ensembles at 5 h and a height of 0.5 km. (d)–(f) Rotational wind speed (colors) and rotational wind vectors for the same members, time, and height. All fields have been filtered to remove wavelengths shorter than 32 km. The member selected from the 10L, 20L, and 30L ensembles corresponds to Figs. 2d, 3d, and 4d, respectively.

spectra are similar to those at the smallest scales captured in global models (Burgess et al. 2013; Skamarock et al. 2014) or in channel models of baroclinically unstable waves (Waite and Snyder 2013). Among these, the convection-permitting MPAS simulations on a global quasi-uniform hexagonal mesh with 3-km cell spacing (Skamarock et al. 2014) appear to offer the best opportunity for comparison with our

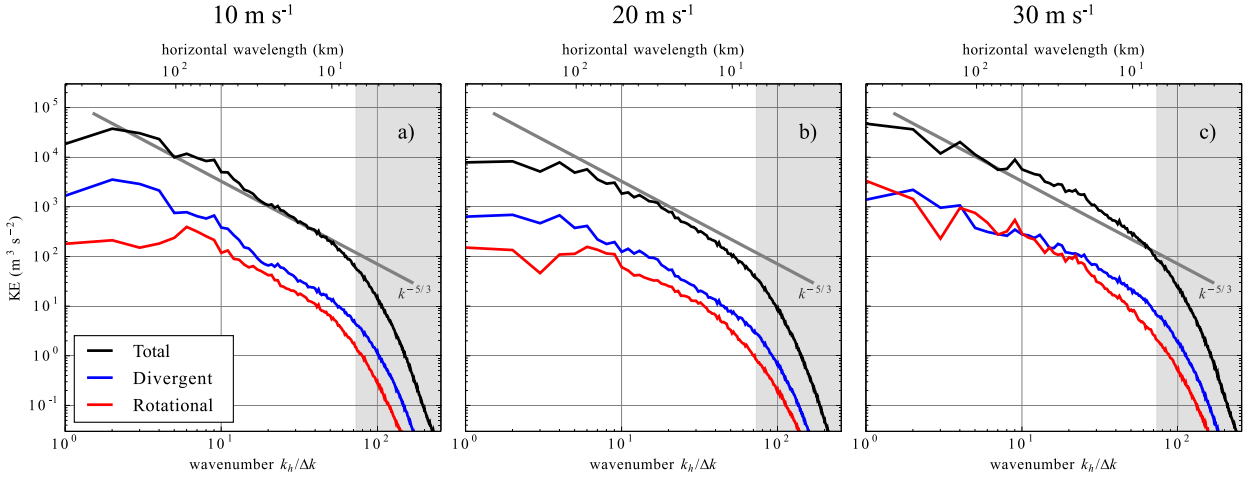

FIG. 15. Total KE spectra at a height of 500 m for (a) the 10L, (b) the 20L, and (c) the 30L ensembles, for the total wind field (black), divergent wind field (blue), and rotational wind field (red) at 5 h into the simulations. The lines for the divergent and rotational spectra are shifted down by a factor of 10 for better visibility. Other details as in Fig. 6.

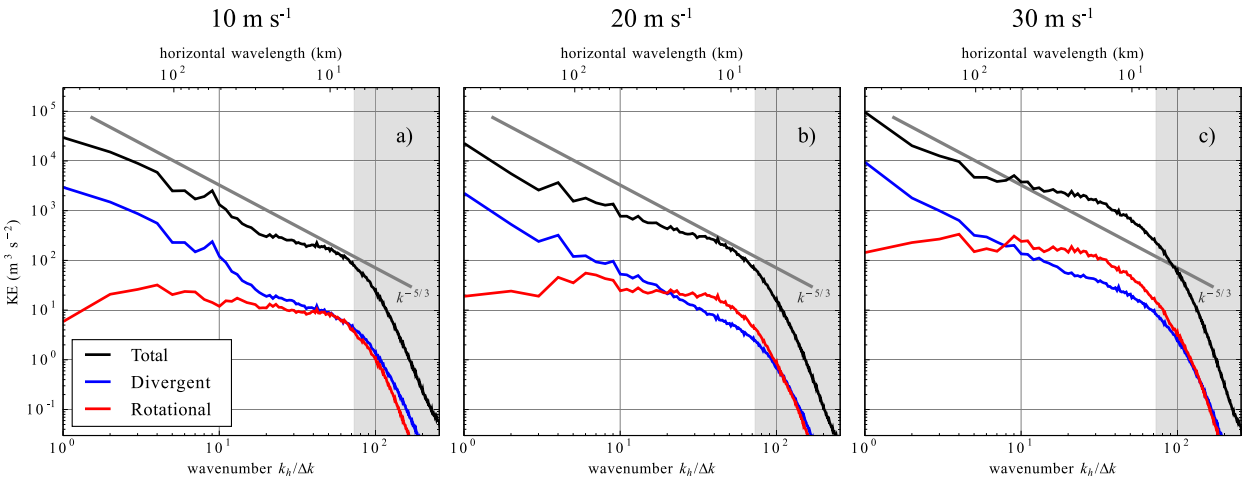

FIG. 16. As in Fig. 15, but at a height of 3 km.

finer-scale MCS simulations. In both MPAS and our simulations, the DKE and RKE have similar magnitudes over a range of the smallest resolved scales in the troposphere, while DKE dominates RKE in the stratosphere.

In our simulations, the DKE spectrum more closely follows a $k^{-5/3}$, or slightly shallower, slope than does the RKE (Figs. 15, 16, 18, 20), as has also been noted in coarser-resolution simulations with parameterized convection (Burgess et al. 2013). Some of the convergence and divergence in our simulations is associated with the convective-system-scale low-level inflow and anvil-level outflow, as evident in Fig. 12, but small-scale gravity waves are likely responsible for the nearly uniform

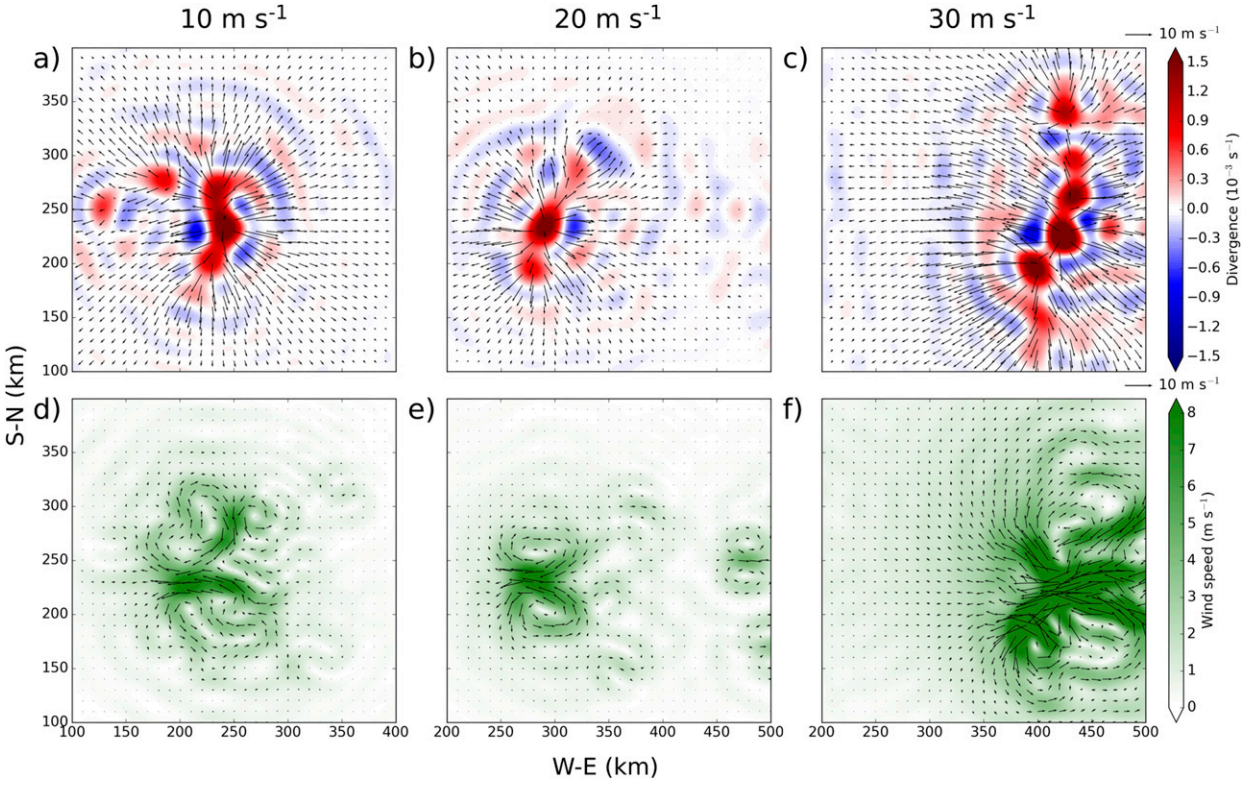

FIG. 17. As in Fig. 14, but at a height of 11 km.

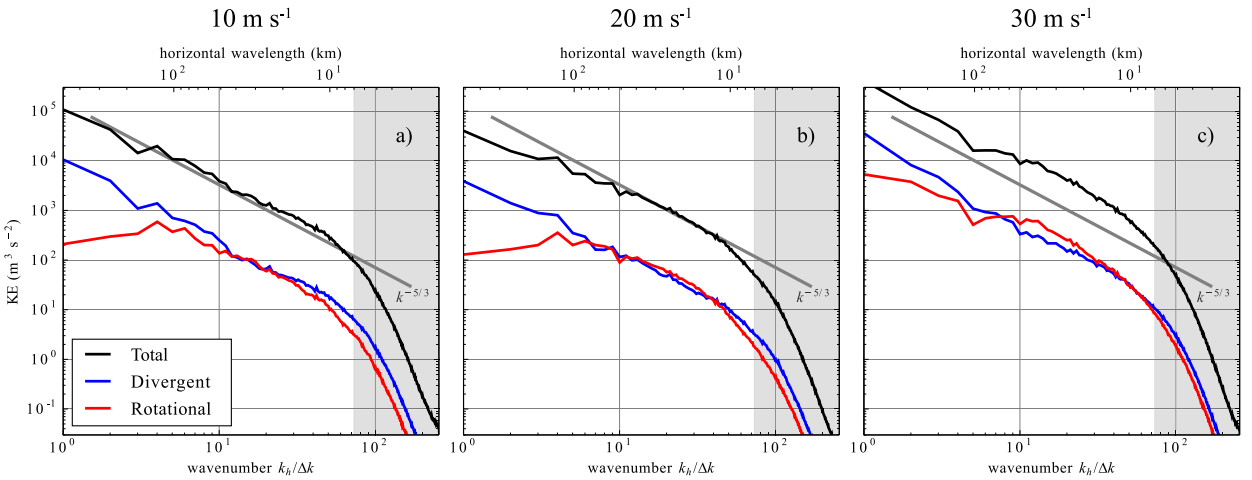

FIG. 18. As in Fig. 15, but averaged over heights of 10–12 km (the anvil level). The total KE lines are the same as the 5-h total KE lines in Figs. 6d–f.

vertical distribution of DKE at wavelengths shorter than 32 km (Fig. 13).

7. Discussion

We showed in section 3 that the predictability lead time of mesoscale convective systems does not depend on the horizontal scale of equal-amplitude initial errors. In the mesoscale, where the background KE follows a $k^{-5/3}$ spectrum, this suggests that small relative errors in initial conditions on the largest mesoscales should have impacts similar to larger relative errors on smaller scales. Durran and Gingrich (2014) compare the relative errors corresponding to equal-amplitude errors in the

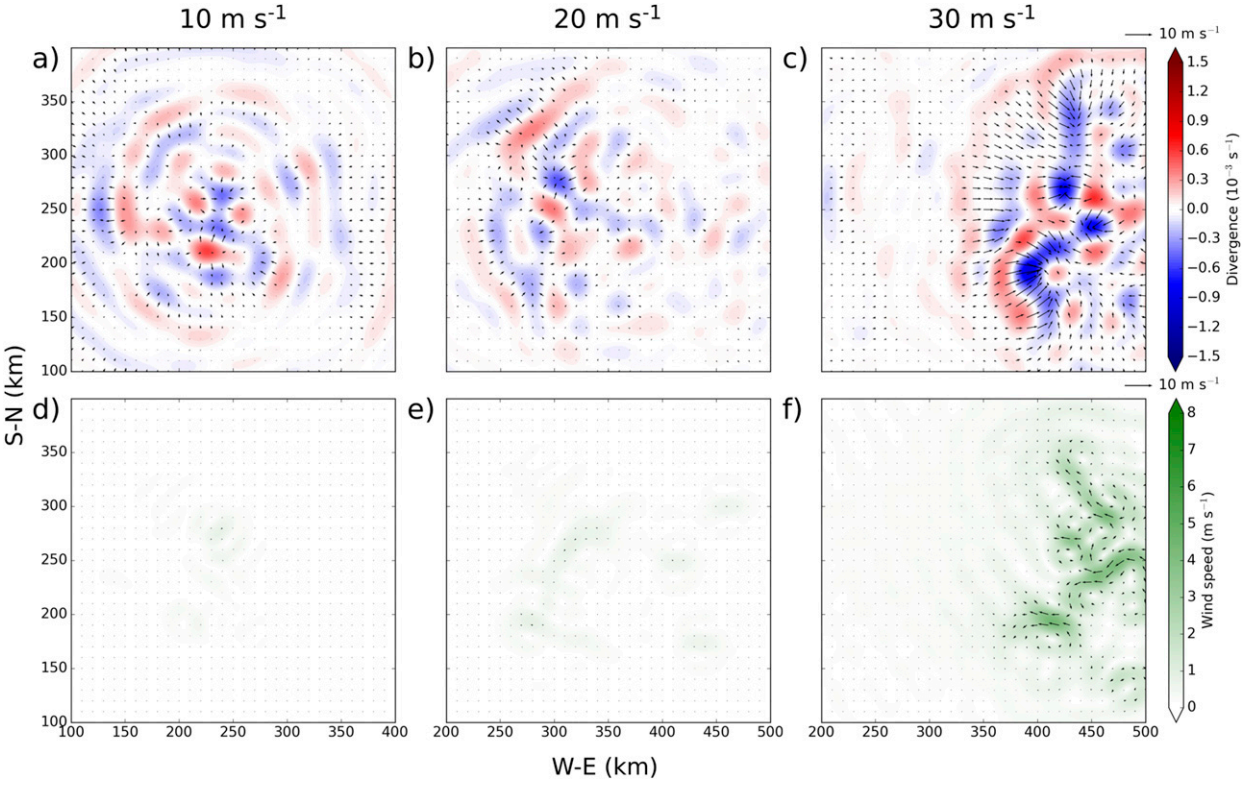

FIG. 19. As in Fig. 14, but at a height of 14 km.

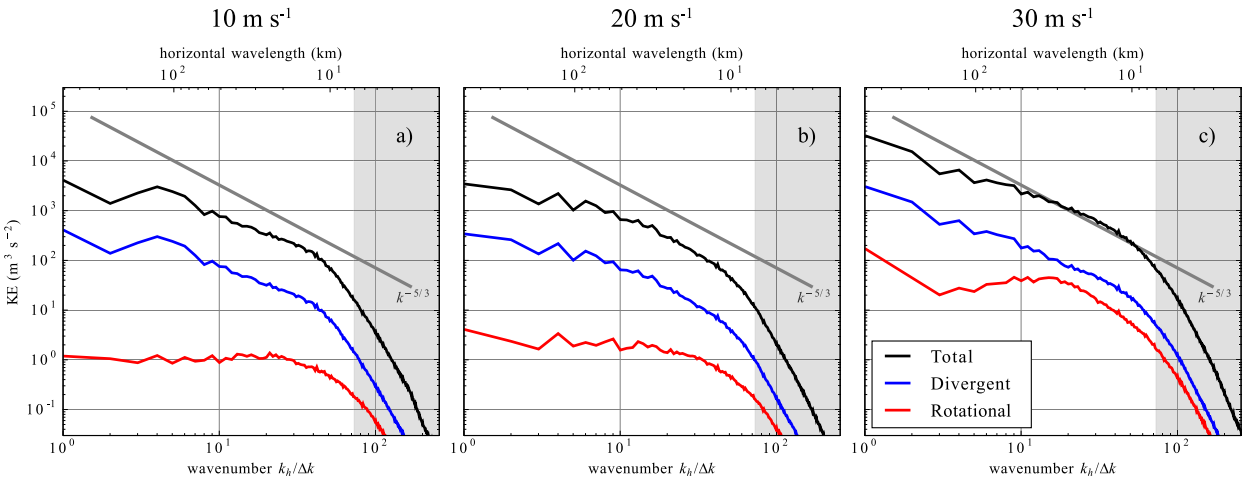

FIG. 20. As in Fig. 15, but averaged over heights of 14–16 km.

velocity field at specific pairs of wavelengths; in the following, we generalize this discussion to relative errors in spectral bands, which are more directly relevant to problems like the formulation of data assimilation strategies. The total KE along a line of length S and the integrated KE spectrum along the same line are connected by Parseval's theorem, which states[10]

$$\int_S u^2(x)\,dx = \int_{-\infty}^{\infty} \hat{u}(k)\hat{u}^*(k)\,dk.$$

Let us denote the contribution to the total KE in the spatial domain from wavenumbers in the interval $[k_1, k_2]$ as

$$E(k_1, k_2) = \frac{1}{2}\int_{k_1}^{k_2} [\hat{u}(k)\hat{u}^*(k) + \hat{v}(k)\hat{v}^*(k)]\,dk. \quad (3)$$

Suppose the KE follows a $k^{-5/3}$ spectrum; then, for some constant α,

$$\hat{u}(k)\hat{u}^*(k) + \hat{v}(k)\hat{v}^*(k) = \alpha k^{-5/3}. \quad (4)$$

Let λ_j be the wavelength corresponding to wavenumber k_j; using (3) and (4), the ratio of the KE in wavenumber band $[k_1, k_2]$ to that in band $[k_3, k_4]$ is

$$\frac{E(k_1, k_2)}{E(k_3, k_4)} = \frac{k_1^{-2/3} - k_2^{-2/3}}{k_3^{-2/3} - k_4^{-2/3}} = \frac{\lambda_1^{2/3} - \lambda_2^{2/3}}{\lambda_3^{2/3} - \lambda_4^{2/3}}. \quad (5)$$

From (5), the ratio of the KE in the 2–4-km band to that in the 200–400-km band (both factor-of-2 changes in wavelength) is 0.0464, implying that the ratio of the background velocities in these bands is 0.215. Thus, the characteristic atmospheric horizontal velocities over the wavelength range of 2–4 km are 21.5% as large as those in the range of 200–400 km, and a 100% error in the 2–4-km band would have the same amplitude (and roughly the same negative impact on predictability) as a 21.5% error in the 200–400-km band. This analysis attaches more significance to small-scale errors than the analysis in Durran and Gingrich (2014) but still implies

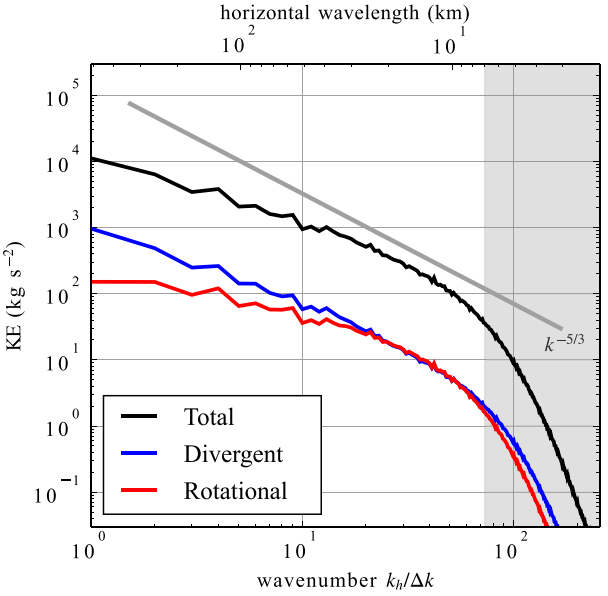

FIG. 21. Density-weighted kinetic energy spectra averaged over $0 \le z \le 15$ km and times 4–6 h for the 20L ensemble: total wind field (black), divergent wind field (blue), and rotational wind field (red). The lines for the divergent and rotational spectra are shifted down by a factor of 10 for better visibility. Other details as in Fig. 6.

[10] For simplicity, we give formulas for a one-dimensional domain, but the argument for two-dimensional spectra such as those used in (2) is virtually identical.

that relative errors at the largest mesoscale wavelengths must be small before one can expect to gain predictability at lead times of roughly 5 h by incorporating finescale data from sources like radar. If we consider very small-scale disturbances due to butterflies perturbing the atmosphere at wavelengths between 5 and 10 cm, 100% errors on the butterfly scale would correspond to 0.63% errors on the 200–400-km scale. Although this value is larger than obtained by simply comparing relative errors at wavelengths of 400 km and 10 cm (Durran and Gingrich 2014), the spectral band analysis continues to imply that butterflies would not be of practical importance in actual weather forecasts.

8. Conclusions

Ensemble simulations of mesoscale convective systems forced by three environmental wind profiles have been presented to analyze the relative importance of small- and large-scale initial errors on mesoscale predictability. All of the simulations show that, at lead times of 5 h, there is no significant difference in the loss of predictability between ensembles initialized with equal-amplitude absolute errors at wavelengths of 5.7 and 90 km, despite the differences in the evolution of the MCSs under different environmental wind shear. The initial perturbations in our control ensembles were produced by a $0.1\,\mathrm{g\,kg^{-1}}$ amplitude monochromatic square wave of random phase in the surface and near-surface moisture field. The intrinsic predictability of our idealized convective systems was examined by reducing the initial amplitude of these perturbations by factors of 1/5 and 1/25, respectively. Similar error-saturation spectra are produced at forecast lead times of 290, 340, and 360 min as the amplitude of the moisture perturbations are successively reduced from 0.1 to 0.02 to $0.004\,\mathrm{g\,kg^{-1}}$, suggesting a limit of intrinsic predictability at 20-km horizontal scales of a bit more than 6 h. Despite the idealized nature of these simulations, this predictability lead time is roughly consistent with National Atmospheric and Oceanic Administration (NOAA) Hazardous Weather Testbed (HWT) Spring Forecasting Experiment assessments of the practical impact of finescale radar data assimilation on thunderstorm forecasts (Kain et al. 2010; Stratman et al. 2013; Surcel et al. 2015). Nevertheless, as suggested by the range of MCS structures in Figs. 2–4 and determined quantitatively by the error saturation, the large-scale structure of MCSs in $30\,\mathrm{m\,s^{-1}}$ may yet be more predictable than those in less sheared environments.

In the series of ensemble simulations with different initial perturbation amplitudes, as well as the series with different environmental wind shears, the error saturation at 5 h remained insensitive to the horizontal scale of the initial error. The idealized spectral turbulence model of Lorenz is also insensitive to the scale of equal-amplitude initial errors because large-scale errors rapidly propagate downscale where they saturate and then grow through an upscale cascade as if those errors had simply been present in the small scale to begin with (Lorenz 1969; Durran and Gingrich 2014). The initial errors in our ensembles rapidly spread across all scales, both downscale and upscale, but the subsequent error growth is "up amplitude," rather than through a cascade from the smallest scales. Similar patterns of spectral error growth have been observed in several previous studies (Mapes et al. 2008; Durran et al. 2013; Durran and Gingrich 2014), including simulations of deep convection (DW16; Potvin et al. 2017).

Our result that equal-amplitude errors introduce similar losses in predictability independent of scale differs slightly from that of DW16, who found that low-level potential temperature perturbations in a square wave form with $L = 8$ km produced similar error growth to perturbations with $L = 128$ km and one-fourth the initial amplitude. Our current results differ from DW16 because we perturb the moisture field instead of the potential temperature field, we use a different environmental sounding, and we include simple boundary layer friction. The relative rates of error growth due to initial perturbations in various dynamical fields, particularly at different horizontal scales, warrant further study.

As in DW16, the MCSs produced in all simulations generate a background $k^{-5/3}$ KE spectrum, consistent with observations of the atmosphere at similar horizontal wavelengths (Nastrom and Gage 1985; Lindborg 1999; Cho and Lindborg 2001) and those generated by numerous model studies (e.g., Hamilton et al. 2008; Waite and Snyder 2013; Burgess et al. 2013; Skamarock et al. 2014; Sun et al. 2017). The absolute magnitudes of the KE spectra in the 10 and $20\,\mathrm{m\,s^{-1}}$ shear cases happen to be very close to the average values observed between the heights of 9 and 14 km by Nastrom and Gage (1985) (Figs. 18a,b), although our values would decrease if otherwise identical simulations were conducted in larger domains [see (2)].

In our simulations, the disturbance ultimately responsible for creating the $k^{-5/3}$ KE spectrum is clearly deep convection. This is consistent with the general hypothesis of Lilly (1983) that energy injected at small scales by convection is responsible for the $k^{-5/3}$ KE spectrum observed at mesoscale wavelengths, although the analysis by Sun et al. (2017) suggests the detailed dynamical processes differ from the 2D inverse cascade envisioned by Lilly. Instead, Sun et al. (2017) found that the spectrum develops as a result of 1) the buoyant

production of KE over a range of scales with a peak at short wavelengths, 2) a vertical redistribution of this buoyancy-generated KE, and 3) a filling out of the spectrum by nonlinear interactions. Given the similarity of the Sun et al. (2017) simulations to our 20 m s^{-1} shear case, and the similarities among the KE spectra from our simulations in different environmental shears, it is likely that the same processes are acting in our simulations.

The vertical distribution of the KE shows a pronounced maximum at anvil-outflow level, which, in the 10 and 20 m s^{-1} shear cases, is strongly dominated by the divergent component of the wind (DKE) on scales similar to or larger than the MCS itself. In agreement with convection-permitting global MPAS simulations (Skamarock et al. 2014), at shorter wavelengths DKE and RKE have similar magnitudes in the upper troposphere, while DKE dominates RKE in the stratosphere. In the 30 m s^{-1} shear case, the magnitude of the RKE is enhanced relative to the DKE by the stronger shear, likely because of stronger tilting of environmental horizontal vorticity into the vertical by the convective updrafts. In all our ensembles, the DKE spectrum more closely follows a $k^{-5/3}$, or slightly shallower, slope than does the RKE, as has also been noted in coarser-resolution simulations with parameterized convection (Burgess et al. 2013). At wavelengths shorter than 32 km, the DKE exhibits a nearly uniform distribution with height, suggesting that vertical transport by gravity waves may play a role in homogenizing this component of the KE spectrum.

The universality of our results across all ensembles, with differences only in a few details, suggests that mesoscale structures with horizontal scales between 100 and 400 km exert a significant control on deep convective systems. Similarly, Potvin et al. (2017) found that forecasts of supercells were relatively insensitive to the inclusion of initial conditions at fine scales less than 16 km. Nevertheless, many other factors important in real-world weather forecasts are neglected in our idealized model, including the incorporation of realistic synoptic-scale forcing, a detailed representation of boundary layer processes, the Coriolis force, topography, and radiative effects. To address these limitations, further studies of the predictability in real-world simulations using the Weather Research and Forecasting (WRF) Model initialized prior to actual severe weather events are being conducted by the authors.

Acknowledgments. The authors gratefully acknowledge discussions with Alex Reinecke and Jim Doyle. The paper was improved by comments from Corey Potvin and two anonymous reviewers. This research is funded by Grant N000141410287 from the Office of Naval Research (ONR). J. A. Weyn was partly supported by the Department of Defense (DoD) through the National Defense Science and Engineering Graduate (NDSEG) Fellowship Program. The simulations were conducted on Garnet, a supercomputer at the Engineer Research and Development Center (ERDC) DoD Supercomputing Resource Center (DSRC).

REFERENCES

Bluestein, H. B., 1993: *Synoptic-Dynamic Meteorology in Midlatitudes*. Vol. II. Oxford University Press, 608 pp.

Bougeault, P., 1983: A non-reflective upper boundary condition for limited-height hydrostatic models. *Mon. Wea. Rev.*, **111**, 420–429, doi:10.1175/1520-0493(1983)111<0420:ANRUBC>2.0.CO;2.

Burgess, B. H., A. R. Erler, and T. G. Shepherd, 2013: The troposphere-to-stratosphere transition in kinetic energy spectra and nonlinear spectral fluxes as seen in ECMWF analyses. *J. Atmos. Sci.*, **70**, 669–687, doi:10.1175/JAS-D-12-0129.1.

Cho, J. Y. N., and E. Lindborg, 2001: Horizontal velocity structure functions in the upper troposphere and lower stratosphere: 1. Observations. *J. Geophys. Res.*, **106**, 10 223–10 232, doi:10.1029/2000JD900814.

Durran, D. R., and J. B. Klemp, 1983: A compressible model for the simulation of moist mountain waves. *Mon. Wea. Rev.*, **111**, 2341–2361, doi:10.1175/1520-0493(1983)111<2341:ACMFTS>2.0.CO;2.

——, and M. Gingrich, 2014: Atmospheric predictability: Why butterflies are not of practical importance. *J. Atmos. Sci.*, **71**, 2476–2488, doi:10.1175/JAS-D-14-0007.1; Corrigendum, **72**, 3290, doi:10.1175/JAS-D-14-0377.1.

——, and J. A. Weyn, 2016: Thunderstorms do not get butterflies. *Bull. Amer. Meteor. Soc.*, **97**, 237–243, doi:10.1175/BAMS-D-15-00070.1.

——, P. A. Reinecke, and J. D. Doyle, 2013: Large-scale errors and mesoscale predictability in Pacific Northwest snowstorms. *J. Atmos. Sci.*, **70**, 1470–1487, doi:10.1175/JAS-D-12-0202.1.

Gaberšek, S., and D. R. Durran, 2006: Gap flows through idealized topography. Part II: Effects of rotation and surface friction. *J. Atmos. Sci.*, **63**, 2720–2739, doi:10.1175/JAS3786.1.

Hamilton, K., Y. O. Takahashi, and W. Ohfuchi, 2008: Mesoscale spectrum of atmospheric motions investigated in a very fine resolution global general circulation model. *J. Geophys. Res.*, **113**, D18110, doi:10.1029/2008JD009785.

Hohenegger, C., and C. Schär, 2007: Predictability and error growth dynamics in cloud-resolving models. *J. Atmos. Sci.*, **64**, 4467–4478, doi:10.1175/2007JAS2143.1.

Kain, J. S., and Coauthors, 2010: Assessing advances in the assimilation of radar data and other mesoscale observations within a collaborative forecasting–research environment. *Wea. Forecasting*, **25**, 1510–1521, doi:10.1175/2010WAF2222405.1.

Klemp, J. B., and D. R. Durran, 1983: An upper boundary condition permitting internal gravity wave radiation in numerical mesoscale models. *Mon. Wea. Rev.*, **111**, 430–444, doi:10.1175/1520-0493(1983)111<0430:AUBCPI>2.0.CO;2.

Lilly, D. K., 1983: Stratified turbulence and the mesoscale variability of the atmosphere. *J. Atmos. Sci.*, **40**, 749–761, doi:10.1175/1520-0469(1983)040<0749:STATMV>2.0.CO;2.

——, G. Bassett, K. Droegemeier, and P. Bartello, 1998: Stratified turbulence in the atmospheric mesoscales. *Theor. Comput. Fluid Dyn.*, **11**, 139–153, doi:10.1007/s001620050085.

Lindborg, E., 1999: Can the atmospheric kinetic energy spectrum be explained by two-dimensional turbulence? *J. Fluid Mech.*, **388**, 259–288, doi:10.1017/S0022112099004851.

Lorenz, E. N., 1969: The predictability of a flow which possesses many scales of motion. *Tellus*, **21**, 289–307, doi:10.3402/tellusa.v21i3.10086.

Mapes, B., S. Tulich, T. Nasuno, and M. Satoh, 2008: Predictability aspects of global aqua-planet simulations with explicit convection. *J. Meteor. Soc. Japan*, **86A**, 175–185, doi:10.2151/jmsj.86A.175.

Nastrom, G. D., and K. S. Gage, 1985: A climatology of atmospheric wavenumber spectra of wind and temperature observed by commercial aircraft. *J. Atmos. Sci.*, **42**, 950–960, doi:10.1175/1520-0469(1985)042<0950:ACOAWS>2.0.CO;2.

Potvin, C. K., E. M. Murillo, M. L. Flora, and D. M. Wheatley, 2017: Sensitivity of supercell simulations to initial-condition resolution. *J. Atmos. Sci.*, **74**, 5–26, doi:10.1175/JAS-D-16-0098.1.

Rotunno, R., and C. Snyder, 2008: A generalization of Lorenz's model for the predictability of flows with many scales of motion. *J. Atmos. Sci.*, **65**, 1063–1076, doi:10.1175/2007JAS2449.1.

Skamarock, W. C., 2004: Evaluating mesoscale NWP models using kinetic energy spectra. *Mon. Wea. Rev.*, **132**, 3019–3032, doi:10.1175/MWR2830.1.

——, S.-H. Park, J. B. Klemp, and C. Snyder, 2014: Atmospheric kinetic energy spectra from global high-resolution nonhydrostatic simulations. *J. Atmos. Sci.*, **71**, 4369–4381, doi:10.1175/JAS-D-14-0114.1.

Stratman, D. R., M. C. Coniglio, S. E. Koch, and M. Xue, 2013: Use of multiple verification methods to evaluate forecasts of convection from hot- and cold-start convection-allowing models. *Wea. Forecasting*, **28**, 119–138, doi:10.1175/WAF-D-12-00022.1.

Sun, Y. Q., R. Rotunno, and F. Zhang, 2017: Contributions of moist convection and internal gravity waves to building the atmospheric −5/3 kinetic energy spectra. *J. Atmos. Sci.*, **74**, 185–201, doi:10.1175/JAS-D-16-0097.1.

Surcel, M., I. Zawadzki, and M. K. Yau, 2015: A study on the scale dependence of the predictability of precipitation patterns. *J. Atmos. Sci.*, **72**, 216–235, doi:10.1175/JAS-D-14-0071.1.

Trapp, R. J., and M. L. Weisman, 2003: Low-level mesovortices within squall lines and bow echoes. Part II: Their genesis and implications. *Mon. Wea. Rev.*, **131**, 2804–2823, doi:10.1175/1520-0493(2003)131<2804:LMWSLA>2.0.CO;2.

Waite, M. L., 2016: Dependence of model energy spectra on vertical resolution. *Mon. Wea. Rev.*, **144**, 1407–1421, doi:10.1175/MWR-D-15-0316.1.

——, and C. Snyder, 2013: Mesoscale energy spectra of moist baroclinic waves. *J. Atmos. Sci.*, **70**, 1242–1256, doi:10.1175/JAS-D-11-0347.1.

Wandishin, M. S., and D. J. Stensrud, 2008: On the predictability of mesoscale convective systems: Two-dimensional simulations. *Wea. Forecasting*, **23**, 773–785, doi:10.1175/2008WAF2007057.1.

Weisman, M. L., and J. B. Klemp, 1982: The dependence of numerically simulated convective storms on vertical wind shear and buoyancy. *Mon. Wea. Rev.*, **110**, 504–520, doi:10.1175/1520-0493(1982)110<0504:TDONSC>2.0.CO;2.

——, and R. J. Trapp, 2003: Low-level mesovortices within squall lines and bow echoes. Part I: Overview and dependence on environmental shear. *Mon. Wea. Rev.*, **131**, 2779–2803, doi:10.1175/1520-0493(2003)131<2779:LMWSLA>2.0.CO;2.

Zhang, D., and R. A. Anthes, 1982: A high-resolution model of the planetary boundary layer—Sensitivity tests and comparisons with SESAME-79 data. *J. Appl. Meteor.*, **21**, 1594–1609, doi:10.1175/1520-0450(1982)021<1594:AHRMOT>2.0.CO;2.

Zhang, F., A. M. Odins, and J. W. Nielsen-Gammon, 2006: Mesoscale predictability of an extreme warm-season precipitation event. *Wea. Forecasting*, **21**, 149–166, doi:10.1175/WAF909.1.